Meccanica (2021) 56:2575–2598
https://doi.org/10.1007/s11012-021-01388-2

On the symmetries of the origami waterbomb pattern: kinematics and mechanical investigations

Larissa M. Fonseca · Marcelo A. Savi

Received: 2 November 2020 / Accepted: 7 June 2021 / Published online: 21 July 2021

Abstract Origamis are becoming the inspiration of new adaptive structures applied for several purposes. One of the challenges of the design of the origami inspired structures is to deal with the large number of variables and degrees of freedom (DoFs) associated with such complex structures. Closed tessellations have a reduced number of DoF when compared to the opened ones. Besides, the coupling due to the closure of the tessellation promotes some periodicity along the structure. Symmetric behaviors allow the description of the structure from a unit cell behavior, establishing reduced-order models. This paper investigates the origami waterbomb pattern, exploring the unit cell behavior and its symmetries. Initially, kinematics analysis based on an equivalent mechanism approach establishes a reduced-order model associated with symmetry hypotheses. Afterward, mechanical analysis is investigated using a nonlinear finite element analysis through bar-and-hinge formulation. A comparison between both formulations is performed showing the range of validity of the reduced-order model description. The general conclusions are applied to a cylindrical tessellation under symmetric actuation showing the capability of the reduced-order model for the origami description. Results show that the rigid foldability hypothesis is the essential point for the equivalence between the two descriptions.

Keywords Origamis · Tessellation · Equivalent mechanism · Nonlinear analysis · Kinematic analysis · Symmetries

1 Introduction

Origami is the art of folding a flat paper (2D structure) into various forms (3D structures) following a sequence of folding creases, without stretching, cutting, or gluing other pieces of paper to it. Once that it can be flattened onto a plane without distortion (it has a zero Gaussian curvature) and the 3D form is generated by the process of bending, but not stretching or shrinking [31], origami is a developable surface. Therefore, the concept of origami can be applied to the manufacturing of various complex 3D forms by out-of-plane deformation (bending and folding), from a watertight sheet of hard material such as paper, fabric, plastic, and metal.

Origami description can be made considering either kinematics or mechanical approaches. The mechanical description of the folding process is essentially based

L. M. Fonseca · M. A. Savi (✉)
Center for Nonlinear Mechanics, COPPE – Department of Mechanical Engineering, Universidade Federal do Rio de Janeiro, P.O. Box 68.503, Rio de Janeiro, RJ 21.941.972, Brazil
e-mail: savi@mecanica.coppe.ufrj.br

L. M. Fonseca
e-mail: larissamaciel.lah@gmail.com

on forces and movements, or work and energy, which captures the actual behavior of such slender structures. The folding process usually involves significant geometric nonlinearity, which promotes additional nonlinear behaviors related to the deformation of the panels. If such deformation occurs, the origami is considered a non-rigid one. On the other hand, if no bending is observed during the entire folding process, the origami is classified as a rigid one or rigidly foldable.

The study of origami kinematics is recent and has gotten the attention of researchers from several fields of knowledge [32–35]. A challenging aspect is to obtain a closed-form mathematical description for the folding process, allowing to describe the correlation between a flat sheet and the folded 3D shape. However, this description is mathematically complex and, in some cases, fails to have a necessary flexibility and applicability on real circumstances. Different approaches have been applied varying according to the description needed.

Lang [17, 18] proposed an arithmetic description of origamis using tree theory, reshaping the problem of finding an efficient folding pattern as a succession of nonlinear restrict optimization problems. Belcastro and Hull [1] described the folding process of a flat sheet via piecewise isometries. Another approach is the study of linkages, where the creases are represented by joints and the faces are represented by rigid links [3, 5, 19, 30]. The origami element is then represented by an equivalent mechanism, and its motion is studied with transformation matrixes describing the relative motion between the joints.

The above-described formulations are suitable only for origamis where the rigid foldability hypothesis is valid. Non-rigid origamis present additional degrees of freedom associated with the deformation of the panels and, usually, a mechanical approach is required to fully describe its behavior. One approach is the analysis through finite elements analysis (FEA) considering shell elements [12, 23]. This analysis provides information such as stress distribution, plastic deformations, regions of failure and even vibration modes, but with a high computational cost. Besides, the focus is the general behavior of the origami instead of local deformations.

Liu and Paulino [22] developed a general nonlinear formulation for structural analysis of origami structures considering an origami representation based on the bar-and-hinge model proposed by Schrenk and Guest [29]. This formulation assumes that both the material and the folding process have nonlinearities, consisting in a continuous process of quasi-static stabilization at each iteration. This idea was implemented in an open-source code called ‘MERLIN’.

This paper presents a general investigation of the waterbomb origami pattern through the unit cell behavior. Initially, kinematics formulation is developed considering an equivalent mechanism approach of the unit cell. A reduced-order model is proposed in order to describe the origami from its unit cell and symmetry hypotheses. In the sequence, a mechanical description is performed using finite element analysis (FEA). The symmetry hypotheses are evaluated comparing both approaches. The main goal of the paper is the analysis of the symmetry hypotheses, establishing proper conditions for the use of reduced-order models and establishing validity of the rigid-foldability and symmetry hypotheses. The general conclusions are applied to a cylindrical tessellation under symmetric actuation showing the capability of the reduced-order model for the origami description. The closed tessellation analysis allows the evaluation of the strangulation effect that contains local asymmetries.

2 Origamis

An origami structure is built by a tessellation that is a repetition of a unit cell covering the entire sheet. Different unit cells generate different tessellations, with specific properties related to motion, configuration, and actuation [11]. One of the challenges of the origami design is to deal with the large number of variables and degrees of freedom (DoFs) associated with such complex structures. Zhao et al. [36] explored this complexity designing generalized waterbomb tessellations to describe several 3D shapes going from spherical and cylindrical elements to hyperbolic paraboloids and torus, exploring asymmetries on both the pattern design and its shape configuration.

Closed tessellations have a reduced number of DoF when compared to the opened ones. Besides, the coupling due to the closure of the tessellation promotes some periodicity along the structure, which can be described considering different kinds of symmetries. Basically, it is important to consider a local or a global symmetry. A global symmetry is

related to the structure while the local symmetry is related to a unit cell. An origami tessellation can be described as a periodic structure built as the connection of fundamental substructures, called *representative volume element* (RVE). In this regard, it is possible to imagine a total symmetry where the fundamental substructure is the unit cell, or other situations where the fundamental structure is built by a set of unit cells, RVE. Symmetry conditions might need to be associated with both geometrical and mechanical aspects.

The complexity of the origami description increases as the asymmetry of the fundamental representative element accentuates. Therefore, the complexity of the closed tessellation representation relies mostly on the unit cell configuration, regarding its degree of asymmetry.

This paper considers a 6 creased waterbomb pattern (Fig. 1a), which closed tessellation results in a cylindrical-like structure. The natural force associated with the folding process of the closed tessellation tends to generate a conic-like structure (Fig. 1b) [15, 24], which results in local asymmetries even for a symmetric actuation. This conic-like natural force can generate several 3D structures, including a ball-shaped origami (Fig. 1c) and a cylindrical origami (Fig. 1d).

The following sections present a local asymmetry study, evaluating the behavior of a unit cell of the waterbomb pattern considering both kinematics and mechanical approaches.

3 Equivalent mechanism

The analysis of the waterbomb pattern can be based on the hypothesis of rigid origami, where all the deformation is localized on the creases (mountain and valley folds), which means that faces remain flat and undeformed. Therefore, it is possible to analyze the waterbomb unit cell as a mechanism (Fig. 2), where the creases are represented by revolute (or cylindrical) joints and the faces are represented by rigid links. Waterbomb pattern is a spherical mechanism where its movement is restricted to a sphere. Based on that, it can be described as a 6R linkage mechanism [3, 5] with mobility 3 [9, 10]), meaning that 3 variables are necessary to fully describe the position of the mechanism.

The kinematics of a unit cell can be described using this rigid 6R mechanism, allowing to define the number of inputs required to completely describe the unit cell, treated as a linkage mechanism. Therefore, the shape of the unit cell can be completely defined by a required number of inputs or angles between the links, which is defined by the mobility of the mechanism. Chebyschev–Grübler–Kutzbach (C–G–K) equation can be employed for this aim as follows

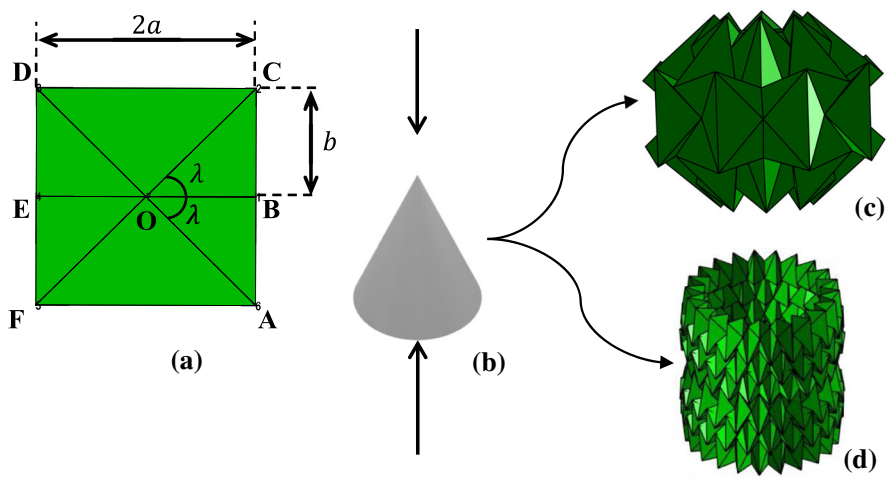

Fig. 1 Waterbomb pattern and natural way of folding. **a** 6 creased waterbomb unit cell with sizes 2a and 2b and inner angle λ, **b** illustration of the geometric relationship between natural force and waterbomb fold pattern, **c** illustration of a closed $m \times n$ waterbomb tessellation, with $m = 3$ lines and $n = 8$ cells in each line; **d** Illustration of a closed $m \times n$ waterbomb tessellation, with $m = 6$ lines and $n = 20$ cells in each line

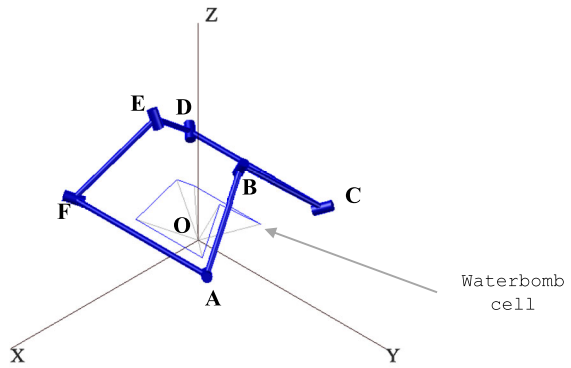

Fig. 2 Equivalent mechanism for the waterbomb pattern described by a unit cell showed in light blue

[13], defining the mobility, M, as a function of the number of links, N, the number of joints, J, and the joint type (planar, spherical, cylindrical). The joint type influences two variables: the generalized displacement of the ith joint, f_i $(i = 1 \ldots J)$, and the constraint parameter related to the mechanism movement, Λ. Therefore,

$$M = \Lambda(N - J - 1) + \sum_{i=1}^{J} f_i. \tag{1}$$

A unit cell of the waterbomb pattern is typically a spherical mechanism ($\Lambda = 3$) with 6 faces or links ($N = 6$) and 6 creases or joints ($J = 6$). Since all the joints are R-type (revolute joints), each one has only one DoF ($f_i = 1$), the rotation around its axis. Therefore, C–G–K equation establishes that $M = 3$, which means that each cell is completely described by three angles, each angle defined between two consecutive links.

The objective of forward kinematics analysis is to determine the cumulative effect of the entire set of joint variables and the mechanism configuration is the output. On the other hand, the objective of the inverse kinematics is to determine the individual values for each joint that result in a specific configuration, and therefore, the mechanism configuration is the input. This paper uses a forward kinematics formulation to evaluate the mechanism configuration. A proper formulation is chosen to avoid singularities that would cause the inverse problem to be ill-posed. One way to address the problem is the use of dual quaternion method [8], a robust technique that allows to unify the translation and the rotation into one single invariant state. Another formulation involves the use of screw theory applied to the joints, or even the definition of screw polygons [25] and screw triangles [14]. The screw triangles theory, applied by Huang and Chen [14], is focused on the unification of finite and infinitesimal kinematics, that proved to be relevant since the motion of rigid bodies can be described as a serial chain of screws.

The Denavit–Hartenberg (D–H) formulation is employed [6], and the transformation between two consecutive joints i and $i + 1$ is a consequence of two rotations and two translations, resulting in a 4 parameters description for each joint-link pair. Therefore, the transformation matrix from joint i and to joint $i + 1$ is given by

$${}^{i}T^{i+1} = \begin{bmatrix} \cos(\theta_i)\cos(\theta_i) & \sin(\theta_i)\cos(\alpha_i) & \sin(\theta_i)\sin(\alpha_i) & a_i\cos(\theta_i) \\ \sin(\theta_i) & \cos(\theta_i)\cos(\alpha_i) & -\cos(\theta_i)\sin(\alpha_i) & a_i\sin(\theta_i) \\ 0 & \sin(\alpha_i)\sin(\alpha_i) & \cos(\alpha_i) & R_i \\ 0 & 0 & 0 & 1 \end{bmatrix} \tag{2}$$

where α_i is the angular distance between two consecutive joints, from z_i to z_{i+1} axis about the x_{i+1} axis; θ_i is the rotation of the ith joint, from x_i to x_{i+1} axis about the z_i axis; a_i is the offset distance measured from the origin O_i to the intersection of axes z_i and x_{i+1}, along the x_{i+1} axis; and R_i is the joint offset, measured as the distance from the i frame to the intersection of axes z_i and x_{i+1}, along the z_i axis (Fig. 3).

The waterbomb pattern has a characteristic that all joints intercept at a common point (point O in Fig. 2), resulting in $a_i = R_i = 0\,(i = 1 \ldots 6)$. In addition, α_i is fixed for each pair of consecutive joints, being associated with the angle λ that defines the shape of

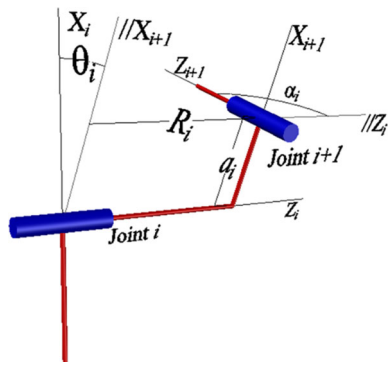

Fig. 3 D–H parameters' setup for the mechanism analysis of the waterbomb

the waterbomb cell and, for a squared waterbomb cell, $\lambda = \pi/4$.

The D–H formulation allows the description of each $i \rightarrow i+1$ joint pair through just four parameters and since three of them are constant values, each joint can be represented by one degree of freedom, θ_i, resulting into 6 free variables. Since the waterbomb pattern is related to a closed chain, the last joint is connected to the first one. In this regard, it is not necessary to think about the end-effector, but instead, it is necessary to evaluate the loop closure equation that acts as a restriction, reducing the number of degrees of freedoms and pointing to the mobility 3 mechanism previously analyzed. The loop-closure equation is as follows

$$^{1}\mathbf{T}^{2}\,^{2}\mathbf{T}^{3}\,^{3}\mathbf{T}^{4}\,^{4}\mathbf{T}^{5}\,^{5}\mathbf{T}^{6}\,^{6}\mathbf{T}^{1} = \mathbf{P}(\boldsymbol{\theta}) \tag{3}$$

where $\boldsymbol{\theta} = [\,\boldsymbol{\theta_1} \quad \ldots \quad \boldsymbol{\theta_6}\,]^{T}$ is the vector of θ_i, $i = 1\ldots6$. Besides, once that the first and last joint are connected by a link, the loop-closure equation must satisfy $\boldsymbol{P}(\boldsymbol{\theta}) - \boldsymbol{I} = \boldsymbol{0}$.

By using the transformation matrix presented in Eq. (2) on the loop-closure, Eq. (3), for a waterbomb unit cell, a system composed by 6 variables (θ_i) and 16 equations is obtained, $f_i(\boldsymbol{\theta}) = [\boldsymbol{P}(\boldsymbol{\theta}) - \boldsymbol{I}]_{mn}$, where $i = 4(m-1)+n$, for $m, n = 1\ldots4$. Note that even though both $\boldsymbol{P}(\boldsymbol{\theta})$ and $\boldsymbol{I}$ are squared matrixes with dimension 4, the D–H parameters for a waterbomb unit cell result in $P_{m4} = 0$ and $P_{4n} = 0$ for every $m, n = 1\ldots3$, and $P_{44} = 1$. Therefore, the system of equations is conceived without the last row and the last column of matrix $\boldsymbol{P}(\boldsymbol{\theta})$, resulting in $f_i(\boldsymbol{\theta}) = [\boldsymbol{P}(\boldsymbol{\theta}) - \boldsymbol{I}]_{mn}$, where $i = 3(m-1)+n$, for $m, n = 1\ldots3$.

The system is solved using nonlinear least-square solver, where the system solutions are obtained as the minimization of the vector $\boldsymbol{F}(\boldsymbol{\theta})$, for a vector input $\boldsymbol{\theta}$, given by

$$\begin{aligned} &\mathbf{F}(\boldsymbol{\theta}) = [f_1(\boldsymbol{\theta}) f_2(\boldsymbol{\theta}) \ldots f_9(\boldsymbol{\theta})]^{T} \\ &\min_{\boldsymbol{\theta}} \|\mathbf{F}(\boldsymbol{\theta})\|^{2} = \min_{\boldsymbol{\theta}} \left(\sum_{i=1}^{9} f_i(\boldsymbol{\theta})^{2} \right). \end{aligned} \tag{4}$$

The system solution considers the lower and upper boundaries that define each θ_i range, $[0, \pi]$, with a central method to estimate gradients for the finite difference estimation. The boundaries are used to avoid superposition or penetration of panels, since even though some configurations are allowed in the equivalent mechanism, they are not achievable by the origami unit cell itself, due to these superpositions/penetrations. The solution is considered converged for a threshold of 10^{-15} for both the function, satisfying $f_i(\boldsymbol{\theta}) = [\boldsymbol{P}(\boldsymbol{\theta}) - \boldsymbol{I}]_{mn} \approx 0$, and the variables (θ_i).

3.1 Workspace analysis of the waterbomb unit cell

The mechanism workspace represents a region of movement of the end-effector relative to a referential frame, usually attached to the frame associated with the first linkage. In this subsection, a workspace analysis is carried out considering the motion of the waterbomb unit cell, related to the frame attached to the crease OA.

The origami analysis considers a subset of angles $(\theta_1, \theta_2, \theta_3)$ that, if physically attainable without stretching, twisting, or compressing the links and without penetration of panels, is identified in a feasible region of the 3D space named as workspace. Figure 4a–i presents the waterbomb unit cell workspace, defined by the feasible region generated by giving $(\theta_1, \theta_2, \theta_3)$ in a range $[0, \pi]$. The workspace assumes a spherical configuration, centered at $(0, 0, 0)$. Note that it is composed by two spheres: an inner sphere, associated with the motion of vertices B and E, and an outer sphere, associated with motion of vertices C, D and F, being vertex A an inertial point located in the outer sphere.

The workspace contained in Fig. 4 corresponds to the dots, being formed through a contribution of the combined motion of vertices B to F of the waterbomb cell, where vertex A is the inertial one. The waterbomb cell is represented through the connection of the position of each vertex on the workspace where vertices A, C, D and F belong to the outer sphere with radius $OA = OC = OD = OF = b\sqrt{2}$, and vertices B and E belong to the inner sphere with radius $OB = OE = b$. The points in the workspace should not be considered individually, but as a set of 6 points that define the unit cell. As examples, 9 sets are selected where each one corresponds to a subset of angles $(\theta_1, \theta_2, \theta_3)$ given as an input and a subset of angles $(\theta_4, \theta_5, \theta_6)$ that corresponds to the output. The subset for each case in Fig. 4a–i is shown in Table 1, along with the converged remaining three angles,

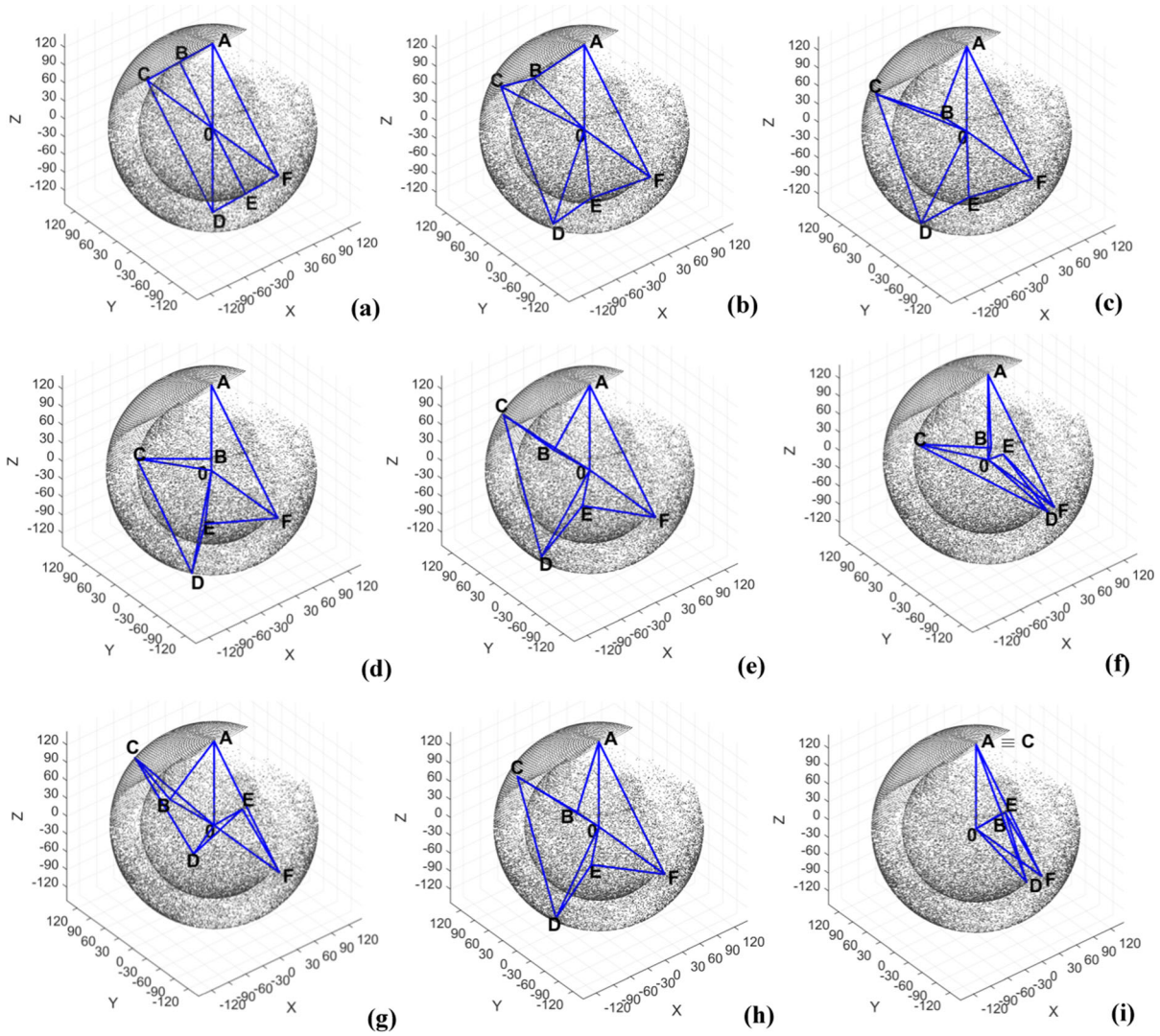

Fig. 4 Different representations of the unit cell shape configurations for distinct values of the input angles $(\theta_1, \theta_2, \theta_3)$. The waterbomb cell is represented through the connection of the position of each vertex on the workspace where vertices A, C, D and F belong to the outer sphere with radius OA = OC = OD = OF = $b\sqrt{2}$, and vertices B and E belong to the inner sphere with radius OB = OE = b (see Fig. 1a)

Table 1 Subsect of input angles $(\theta_1, \theta_2, \theta_3)$ and numerically converged remaining three angles $(\theta_4, \theta_5, \theta_6)$

	a	*b*	*c*	*d*	*e*	*f*	*g*	*h*	*i*
θ_1	0	30	90	90	95	95	95	105	180
θ_2	0	45	75	75	110	145	170	105	180
θ_3	0	30	75	130	90	145	80	105	175
θ_4	0	22.70	19.51	68.00	63.52	174.04	100.90	66.60	165.90
θ_5	0	48.28	49.30	74.86	99.44	153.67	173.72	96.64	175.00
$\boldsymbol{\theta_6}$	0	34.56	111.11	140.73	98.11	144.33	83.09	116.49	170.04

Table 1. Figure 4a shows the particular case where the waterbomb is fully unfolded.

A different perspective of the workspace is now of concern highlighting the vertices on the workspace. Figure 5 highlights each joint-linkage pair, considering a referential frame at crease *OA* (joint *A*). It should be highlighted that superposition and penetration of panels define unfeasible regions associated with an empty space on the workspace. In other words, holes and isolated groups are generated in the workspace due to unfeasible configurations. These isolated groups represent a peculiar set of tridimensional configurations achieved by the waterbomb cell, where the structure has an inversion of crease type or is on the verge of a panel penetration. Any configuration that would be in between these isolated components results in a cell with a superposition and/or penetration of panels and, therefore, are not contemplated in the workspace. A connection between these isolated components requires a deformation on at least one panel that is not feasible for the equivalent mechanism description due to geometrical restrictions.

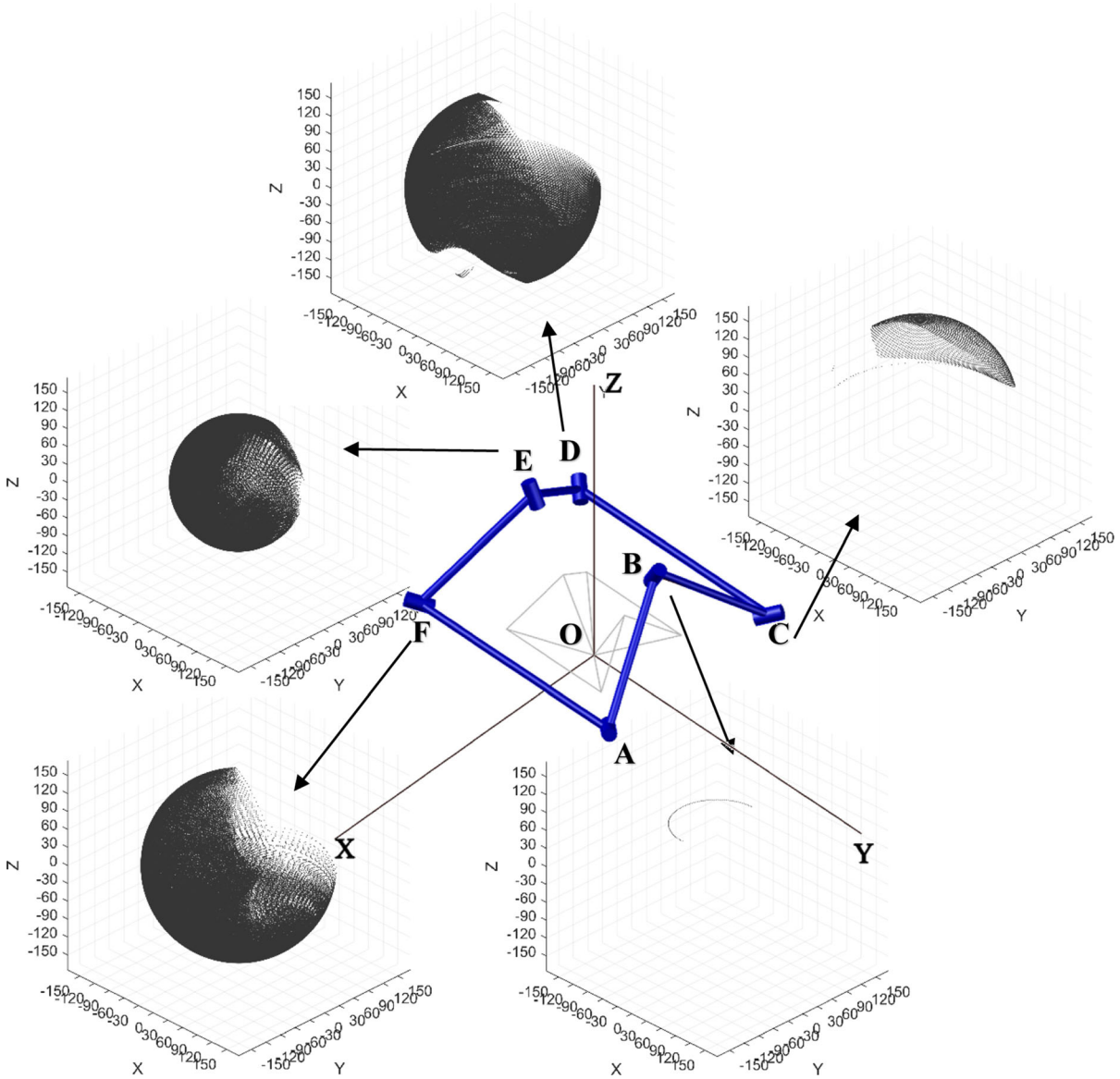

Fig. 5 Workspace for each joint-linkage pair of the waterbomb cell, considering the referential frame at joint A (crease OA)

3.2 Symmetries of the waterbomb unit cell

The mobility of the unit cell mechanism can be reduced by imposing symmetry conditions that can be associated with either the actuation or mechanical restriction imposed to the origami. The actuation providing symmetric responses is related to external forces that are applied in such a way that preserves the symmetry. The mechanical restriction can be achieved by considering some displacement constraint.

By observing the unit cell in Fig. 6a, three symmetry plans can be defined, where the first one leads to a symmetry plane type Π_1 (with mobility 2), the second one leads to a symmetry plane type Π_2 (with mobility 2) and the third one leads to a symmetry plane type Π_3, which represents the cell with a symmetric behavior (with mobility 1). The first symmetry plane is obtained through a diagonal of the unit cell, either AD or CF (Π_1), resulting in $\theta_i = \theta_{i+3}$, for $i = 1...3$. The second symmetry plane is obtained through the plane containing OBE (Π_2), resulting in $\theta_3 = \theta_5$ and $\theta_2 = \theta_6$. The third symmetry plane is obtained by connecting the middle points of the links CD and AF such that $AF \parallel CD$ (Π_3), resulting in $\theta_2 = \theta_3 = \theta_5 = \theta_6$ and $\theta_1 = \theta_4$. Note that this third case has a shape that can be fully described by only one angle, since the origami is fully symmetric (mobility 1). In addition, the shapes resulting from Π_3 can be considered as a subset of the shapes resulting from both Π_1 and Π_2, as can be observed in Fig. 7a–c, where the intersection between the workspaces considering Π_1 and Π_2 is the workspace considering Π_3.

Plane-symmetry constrains mostly the workspace of the joint 4, associated with the crease OE. The original spherical surface covered by the motion of crease OE (see Fig. 5) is now reduced to a single spherical arc for all three cases, Π_1, Π_2 and Π_3. It is important to remember that the referential frame associated with the crease OA is considered as the inertial frame. The study of the symmetry cases is an interesting strategy to design the actuation of the origami. This advantage is clear when observing the change on the workspace of node E from a general case (Fig. 5) to the plane-symmetric cases (Fig. 7). If the objective is to constrain the waterbomb to a symmetric or quasi-symmetric motion, it suffices to control the motion of node E, keeping it in a spherical arc, as shown in Fig. 5. Additionally, it is possible to notice that for all three plane-symmetric and symmetric cases the workspace of node F is confined within a single dot in space. This immovability of node F is the main reason that makes node E behaves the same way as node B, describing just a single arc in space.

Symmetry assumptions can be employed to reduce the necessary equations for the origami description, leading to a simplified formulation. Another way to obtain the equations for the symmetric case is the use of other formulations such as spherical trigonometry, since the waterbomb is a spherical mechanism [2, 4, 7, 9, 10].

The next section presents the mechanical description of the origami unit cell using FEA. A comparison is performed between kinematics and mechanical formulations.

4 Finite element analysis (FEA)

Origami description based on the kinematics analysis focus on the rigid origami hypothesis where the folding process occurs only on the creases and the faces remain flat (no bending is considered). This type of description allows one to use closed-form expressions for the equivalent mechanism.

Mechanical behavior of the origami takes place when deformation on the faces is allowed, establishing a non-rigid origami analysis. FEA is an approach to deal with this, contemplating all possible deformations and twists on the structure. However, this type of description is usually related to a high computational cost.

Schrenk and Guest [29] proposed a simplified bar-ang-hinge model for the structural analysis of origami structures, including some bending through virtual folds added on the faces with a low computational cost. Nevertheless, this formulation is based on infinitesimal displacements and deformations and origami description is essentially based on large displacements. Liu and Paulino [22] developed a formulation that combines a simplified analysis approach with the ability to describe either small or large configurational transformations with a considerably small computational cost. The Merlin Code proposed in this reference is employed here for FEA, with a modification on the deformation description, described in the sequence.

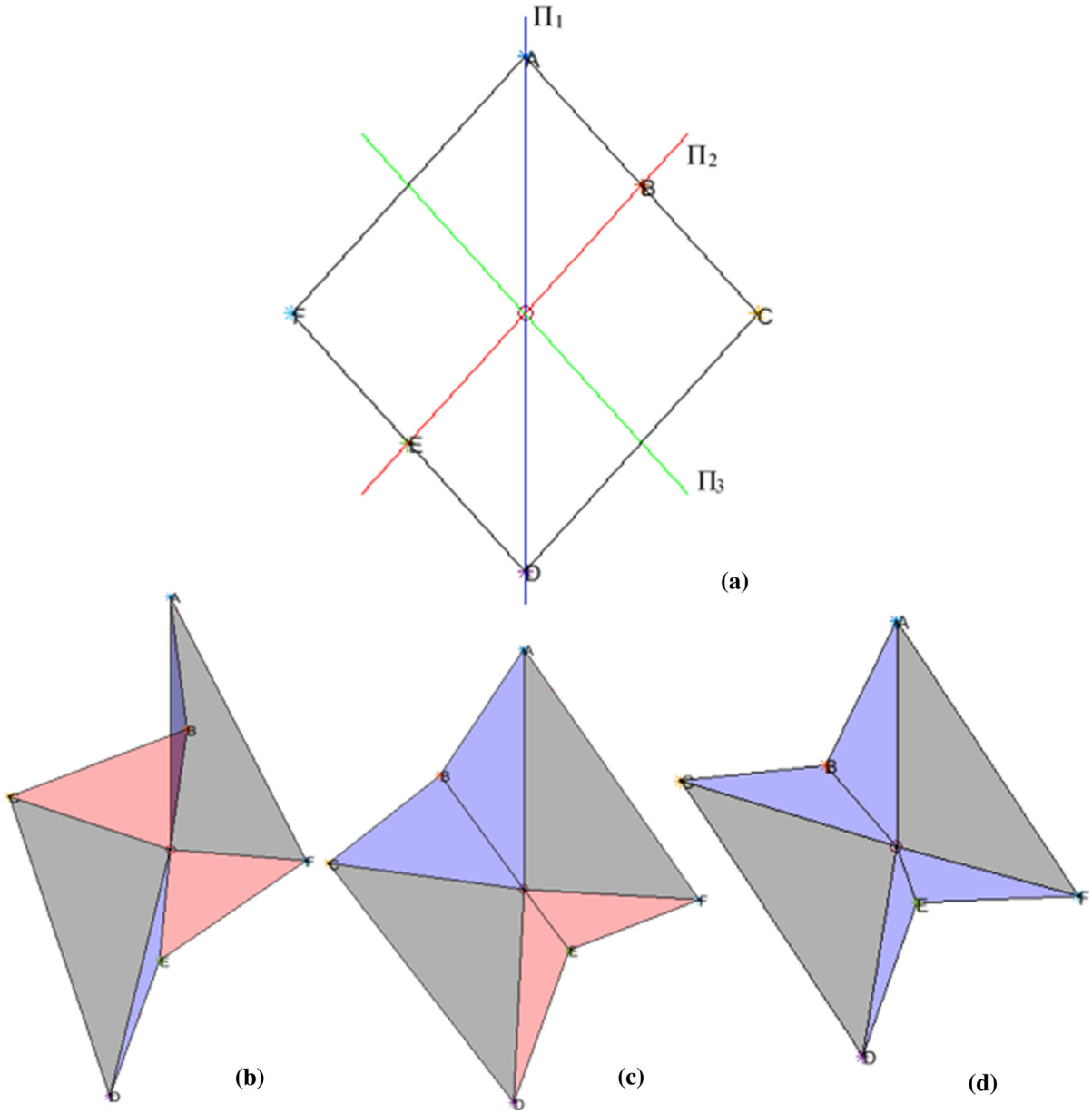

Fig. 6 Symmetry conditions on a waterbomb unit cell: **a** plans of symmetry, **b** configuration related to Case Π_1, with mobility 2, **c** configuration related to Case Π_2, with mobility 2, **d** symmetric configuration related to Case Π_3, with mobility 1

4.1 Formulation

Liu and Paulino [22] developed a finite element representation of the origami considering non-rigid hypothesis and employing the formulation proposed by Schrenk and Guest [29] that describes the origami as a simplified bar-and-hinge structure. In this formulation, the creases act as rotational springs resisting the folding process and the face edges are represented by bar elements (Fig. 8). The panel behavior depends on the bar responses.

The mechanical behavior of origami structures is described assuming quasi-static equilibrium, where the shape change is due to a succession of equilibrium configurations. It is assumed that the total potential energy Φ is the sum of the strain energy stored in bars,

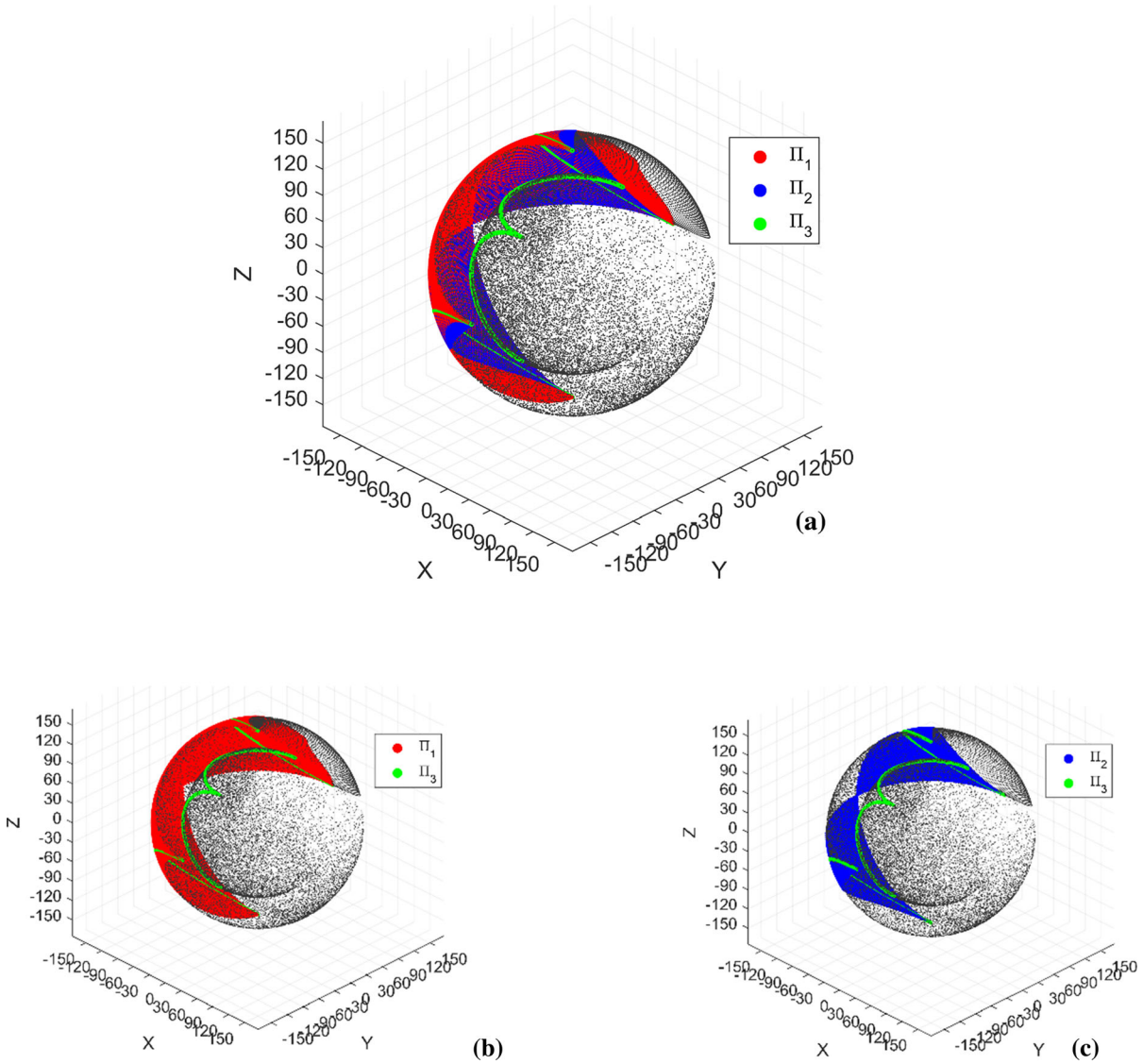

Fig. 7 Workspaces for the plane-symmetry cases Π_1 and Π_2 and the symmetry case Π_3 (**a**). The symmetric case Π_3 is showed superposed to only the plane-symmetric case Π_1 in (**b**), while it is superposed to only the plane-symmetric case Π_3 in (**c**)

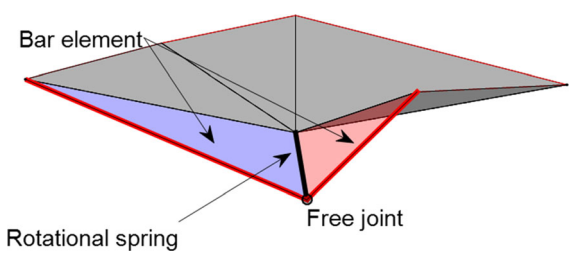

Fig. 8 Bar-and-hinge description of the origami unit cell

U_{bar}, the strain energy stored in folding (torsional springs on the creases) and bending (torsional springs as virtual folds), U_{spr}, and the work done by external loads, V_{ext}, such that, by considering quasi-static equilibrium,

$$\frac{\partial \Phi}{\partial \boldsymbol{u}} = \frac{\partial U_{bar}}{\partial \boldsymbol{u}} + \frac{\partial U_{spr}}{\partial \boldsymbol{u}} - \frac{\partial V_{ext}}{\partial \boldsymbol{u}} = \boldsymbol{T}_{bar} + \boldsymbol{T}_{spr} - \boldsymbol{F}_{ext} = 0 \tag{5}$$

where $\boldsymbol{u}$ is the nodal displacement vector, $\boldsymbol{T}_{bar}$ and $\boldsymbol{T}_{spr}$

are internal forces and $\boldsymbol{F}_{ext}$ is the external load. Internal forces analysis needs to be evaluated considering a proper constitutive equation for both bars and springs. A small perturbation of the externally applied load corresponds to a perturbation in the nodal DoF displacements, such that

$$\boldsymbol{T}_{bar}(\boldsymbol{u}_0) + \boldsymbol{T}_{spr}(\boldsymbol{u}_0) + \left.\frac{\partial\left(\boldsymbol{T}_{bar} + \boldsymbol{T}_{spr}\right)}{\partial \boldsymbol{u}}\right|_{\boldsymbol{u}=\boldsymbol{u}_0} d\boldsymbol{u} = \boldsymbol{F}_{ext} + d\boldsymbol{F}_{ext}. \tag{6}$$

Since Eq. (5) is satisfied by the solution $\boldsymbol{u}_0$, Eq. (6) reduces to

$$d\boldsymbol{F}_{ext} = \left.\frac{\partial\left(\boldsymbol{T}_{bar} + \boldsymbol{T}_{spr}\right)}{\partial \boldsymbol{u}}\right|_{\boldsymbol{u}=\boldsymbol{u}_0} d\boldsymbol{u} = \left[\boldsymbol{K}_{bar}(\boldsymbol{u}_0) + \boldsymbol{K}_{spr}(\boldsymbol{u}_0)\right] d\boldsymbol{u} \tag{7}$$

The bars are described as one-dimensional elements and are modeled as a hyper elastic material represented by a strain energy density function $W(E_x)$, where E_x is the one-dimensional Green–Lagrange strain. The hyper elastic behavior of the bars is described by the constitutive model proposed by Ogden [26], which nonlinearity and generality allows one to represent different materials just by adjusting the model parameters.

The simulations presented in this paper use the N4B5 (4 Nodes, 5 Bars) formulation to describe the virtual folds or bending regions, which divides each quadrilateral panel into two triangles by its shorter diagonal, as demonstrated in Fig. 9. It is important to highlight that the waterbomb pattern has all hinges as folding type, since all panels are triangular.

In addition, N4B5 formulation defines the spring properties by its stiffness $\left(k_{fold} = 0.03\,\mathrm{N\,mm^{-1}}\right)$ and the bar properties by the bar area $(A_{bar} = 0.1\,\mathrm{mm^2})$ and its equivalent stiffness $\left(k_{bar} = 10^4\,\mathrm{N\,mm^{-1}}\right)$. The waterbomb pattern unit cell is defined as a square of side 200 mm.

In order to solve the nonlinear problem, Merlin Code uses a modified generalized displacement control method (MGDCM), a robust approach proposed by Leon et al. [21] that avoids singularities. This method has the main feature to converge the solution even for high values of initial load factor [20]. The original Merlin Code assumes that the load is applied with respect to the undeformed configuration, keeping its initial characteristic during all time steps. Here, this

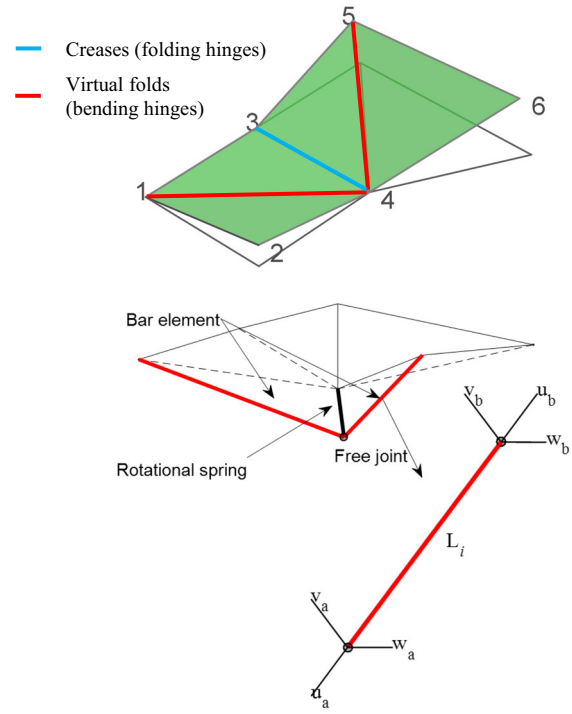

Fig. 9 N4B5 model on an origami pattern with two quadrilateral faces: 1243 and 3465

input load follows the deformed configuration and therefore, follows the node movement. This approach allows a proper description of the origami that does not present any incorrect extra stretching. A workflow for the modified FEA is presented in "Appendix" for a single cell.

5 Numerical simulations

A mechanical analysis of the waterbomb unit cell is now in focus considering numerical simulations using FEA. The study starts with a general visualization of the waterbomb movement under external forces, with evaluation of the deformation of the creases. This analysis compares the kinematics analysis presented in Sect. 3, which assumed a rigid-foldable origami, with the mechanical formulation through Finite Element Analysis (FEA) presented in Sect. 4, which assumed a non-rigid foldable origami in a bar-and-hinge description. A force type input is employed, applied perpendicularly to the panel on the origami deformed configuration, being an adaptative load that

keeps its norm but change the direction at each interaction, following the node movement (Fig. 10a).

All simulations consider the boundary conditions and inputs force as defined in Fig. 10b, where the face AFO (face formed by nodes 5, 6 and 7) is fixed in space and the nodes 1, 2, 3 and 4 (vertices B, C, D and E, respectively) are subjected to external forces.

The folding process of the waterbomb cell is evaluated using FEA for four cases: the plane-symmetric cases (type Π_1 and type Π_2) and symmetric case (Π_3), presented in Sect. 3, and an asymmetric case. These four cases are evaluated with the inputs showed in Table 2, where the input is described by the Node where the Force is being applied and a crease. The crease as an input has two purposes: the first one is to define the Face to which the Force remains perpendicular to, following the Node movement. The second one is the direction of the Force. Thus, a Force applied to Node 1 with Crease identification $7-6$ results in a Force normal to Face *ABO* (face 167) following the motion of Node 1, folding the origami along the crease *OA* such that *OA* is a valley type fold. On the other hand, a Force applied to Node 1 with Crease identification $6-7$ results in a Force normal to Face *ABO* (face 167) following the motion of Node 1, folding the origami along the crease *OA* such that *OA* is a mountain type fold.

At this point, it is important to define the symmetric characteristics and their deviations of the symmetric case. From mechanical point of view, a symmetric behavior of the unit cell can be defined as the case where the creases have identical behaviors, and all mountain type folds present the same absolute deformation along the entire folding process (creases *OA*, *OC*, *OD* and *OF*) and all valley type folds present the same absolute deformation along the entire folding process (creases *OB* and *OE*). A similar observation is made for the angle variation. For the waterbomb unit cell under symmetric behavior, the angle variation of all mountain type folds is the same (angles *A*, *C*, *D* and *F*) along the entire folding process, just as the angle variation of all valley type folds (angles *B* and *E*). Discrepancies along the folding process on both deformation and angle variation are understood as deviation of the symmetric case. This deviated case is identified as a plane-symmetric case if the angle relation is according to either Π_1 or Π_2. Otherwise, it is defined as an asymmetric case.

The bar-and-hinge formulation considers a simplified model of the origami face, where the face deformation is represented by the sum of the contribution of each edge and/or crease deformation. Therefore, a deformation on face *OAF* is represented by the cumulative effect of the deformation on creases *OA* and *OF* and edge *AF*.

Figure 11 shows the motion in space of the four cases presented in Table 2. In addition, Fig. 11 shows the deformation occurring on each one of the six faces of the waterbomb unit cell along the folding process. Figure 11b shows the deformation evolution for the waterbomb origami under symmetric behavior of type Π_3. It is possible to note that faces *OBC* and *ODE* have the same deformation, just as faces *OAB* and *OEF*. More than that, faces *OAB*, *OBC*, *ODE* and *OEF* have the same absolute deformation. Face *OAF* presents a larger deformation related to face *OCD* due to the boundaries applied to the origami, where nodes *A* and *F* have their motion restricted on two out of 3 directions. One deviation from the symmetric case is

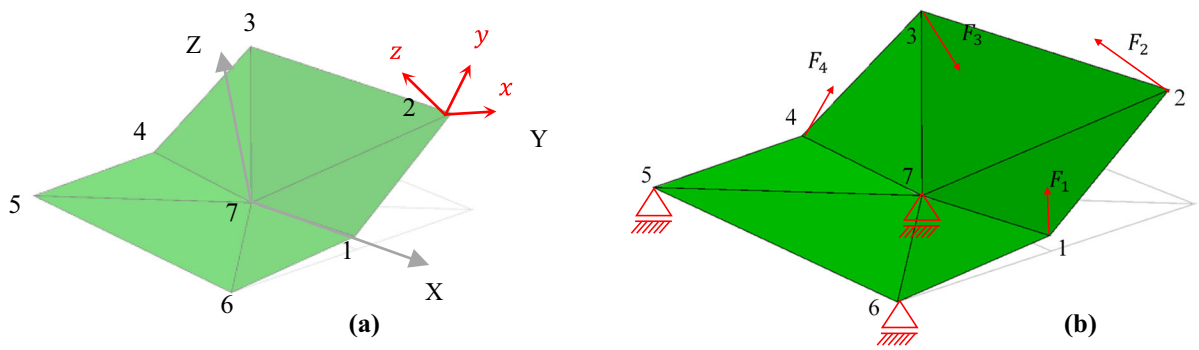

Fig. 10 Force type input applied to the referential frame (x, y, z) that follows the node movement. Axis $z \perp Face_{237}$ and plane *xy* is contained within $Face_{237}$ (**a**); and the origami waterbomb pattern unit cell with boundary conditions and force type input (**b**)

Table 2 Input and final configuration for each one of the four cases: quasi-symmetric (Π_1 and Π_2), symmetric (Π_3) and asymmetric

Case	Π_1			Π_2			Π_3		Asymmetric		
Node	1	4	3	1	4	2	1	4	1	4	2
Crease	7 – 6	7 – 3	7 – 4	7 – 6	5 – 7	7 – 3	7 – 6	5 – 7	7 – 6	5 – 7	3 – 7
Final configuration	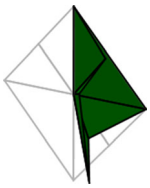			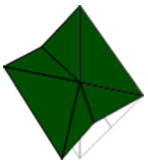			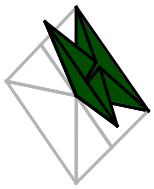		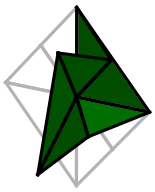		

observed in Fig. 11c, where the waterbomb behaves according to the plane-symmetric case of type Π_2. Note that there is a divergence on the deformation of faces *OBC* and *ODE*, just as for faces *OAB* and *OEF*. An interesting behavior is observed in Fig. 11d, where the waterbomb unit cell behaves according to plane-symmetric case of type Π_1. For this configuration, diagonally opposed faces present the same deformation, by pairs: faces *OAB* and *ODE*, faces *OBC* and *OEF* and faces *OAF* and *OCD*. Finally, for the asymmetric case, shown in Fig. 11e, no symmetry is observed among the deformation of origami unit cell faces.

The folding process can also be evaluated through the inner angles of the origami unit cell, as can be seen in Fig. 12. Note that for the case Π_3, the kinematics formulation can precisely describe the increasing of the angles, even with the creases and edges presenting a large deformation, showed in Fig. 11b, and $A = C = D = F$ and $B = E$ along the entire folding process (Fig. 12a). A similar analysis is performed for the case Π_2, showed in Fig. 12b, where $A = C$ and $D = F$.

As evaluated through the kinematics formulation, when the waterbomb is folding according to case Π_1, the inner angles relate as $\theta_i = \theta_{i+3}$, for $i = 1, 2, 3$. By observing the vertices, this can be translated as $A = D$, $C = F$ and $B = E$. Figure 12c shows the angles evolving with the increment, and it can be noticed that $A \cong D$, $C \cong F$ and $B \cong E$. The deviation can be considered a result of the deformation that happens on the creases (Fig. 11d).

The fourth case, with inner angles showed in Fig. 12d and faces deformation showed in Fig. 11e, represent a general asymmetric motion, with no relation among the angles. Note that in the asymmetric case, the continuous folding of an angle (angle A, for example) might occur in a sequential folding—unfolding—folding of another angle (angle E, for example). This behavior can be seen between time 50 and 100 of Fig. 12d.

A closer observation of the asymmetric case is now performed comparing the path described through kinematics formulation with the path obtained by FEA. Figure 13 establishes a comparison between both formulations. Figure 13a presents the superposed trajectories followed by both cases, showing a good match. This evaluation is ensured by observing the difference on the inner angles for each increment (Fig. 13b). For the kinematics formulation, the input is given by the set of angles $(\theta_1, \theta_2, \theta_3)$, corresponding to the inner angles of vertices B, C and D, respectively. Note that the deviance is smaller than 1 degree (approximately 0.017 rad), meaning that the kinematics formulation can represent the folding process of the waterbomb origami. In other words, the rigid foldability hypothesis is valid.

5.1 Closed waterbomb tessellation: cylindrical origami

After the verification of the rigid foldability hypothesis, it is possible to investigate the description of the origami tessellation by using both the kinematics model and the FEA. Cylindrical origami tessellation is becoming an interesting alternative for the production of stents [16, 27, 28]. This section investigates the cylindrical origami tessellation that allows one to

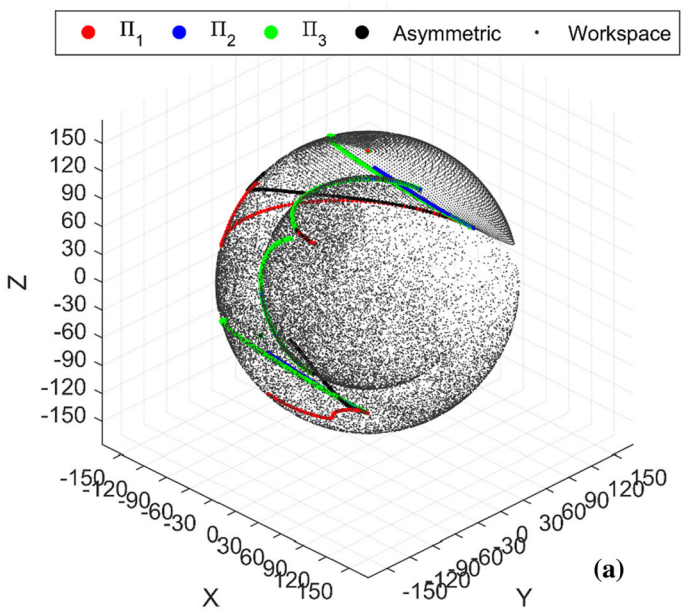
Π1
Π2
Π3
Asymmetric
Workspace
Z
X
Y
(a)

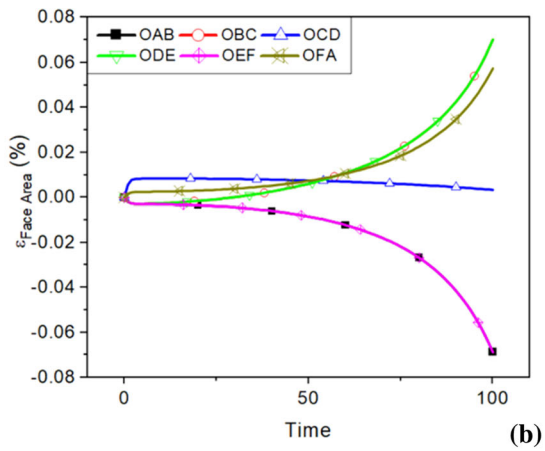
OAB
OBC
OCD
ODE
OEF
OFA
εFace Area (%)
Time
(b)

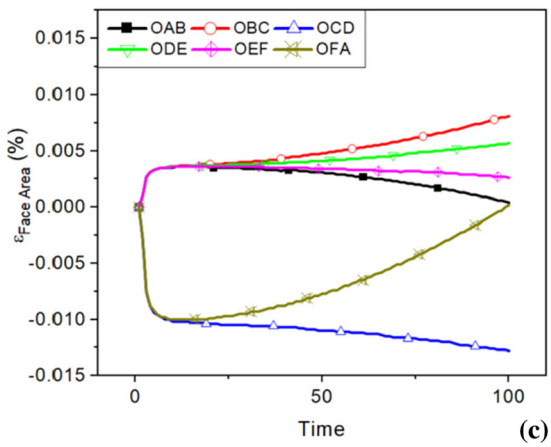
OAB
OBC
OCD
ODE
OEF
OFA
εFace Area (%)
Time
(c)

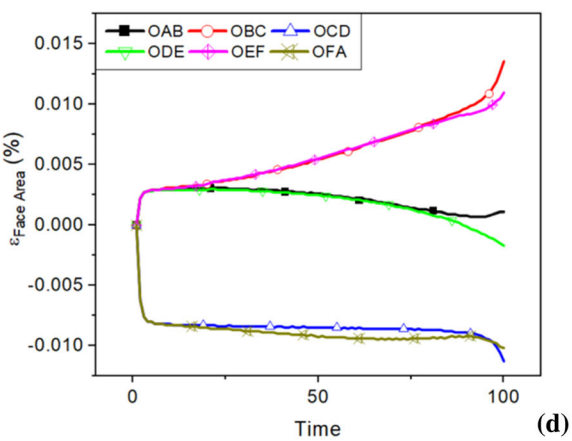
OAB
OBC
OCD
ODE
OEF
OFA
εFace Area (%)
Time
(d)

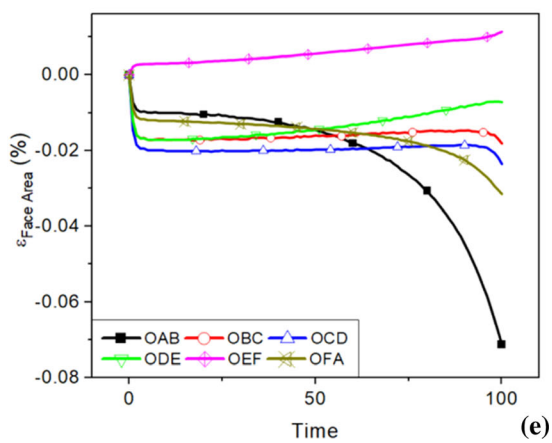
OAB
OBC
OCD
ODE
OEF
OFA
εFace Area (%)
Time
(e)

◀**Fig. 11** Workspace for cases Π_1 and Π_2 and simulations for a generic case (asymmetric), plane-symmetric behavior (Π_1, Π_2) and symmetric behavior (Π_3). The correspondent deformation of each origami face is shown for cases Π_3 (**b**), Π_2 (**c**), Π_1 (**d**) and asymmetric (**e**)

check the conditions on validity of the assumption that a unit cell can represent the general behavior of the structure. The analysis is performed considering a closed $m \times n$ waterbomb tessellation, with m lines and n cells on each line (Fig. 14). The tessellation is

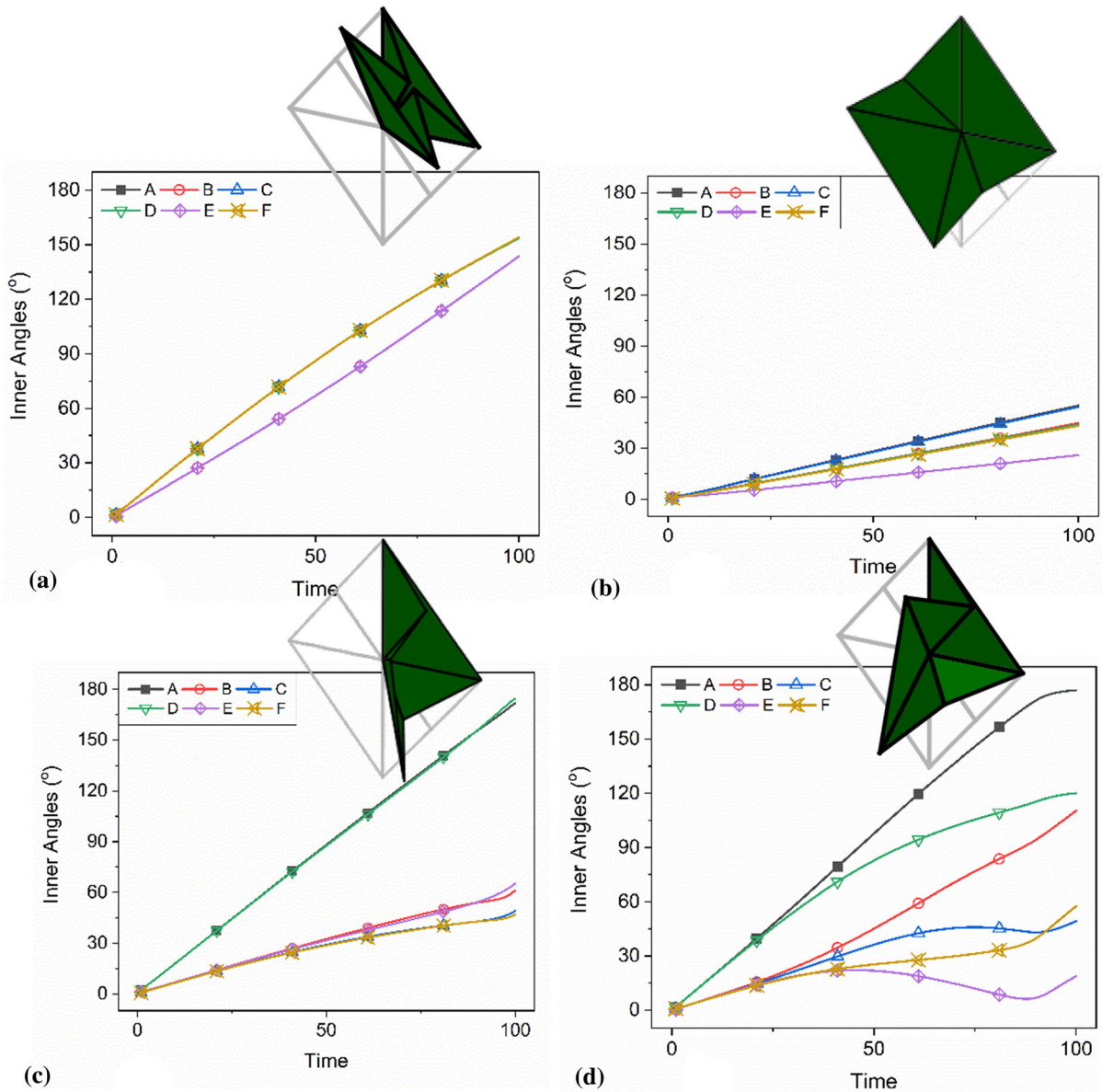

Fig. 12 Evolution of the inner angles of the waterbomb cell with the increment during the folding process, for a folding occurring according to cases Π_3 (**a**), Π_2 (**b**) and Π_1 (**c**), and according to an asymmetric actuation (**d**). The final configuration is also shown in evidence in each case

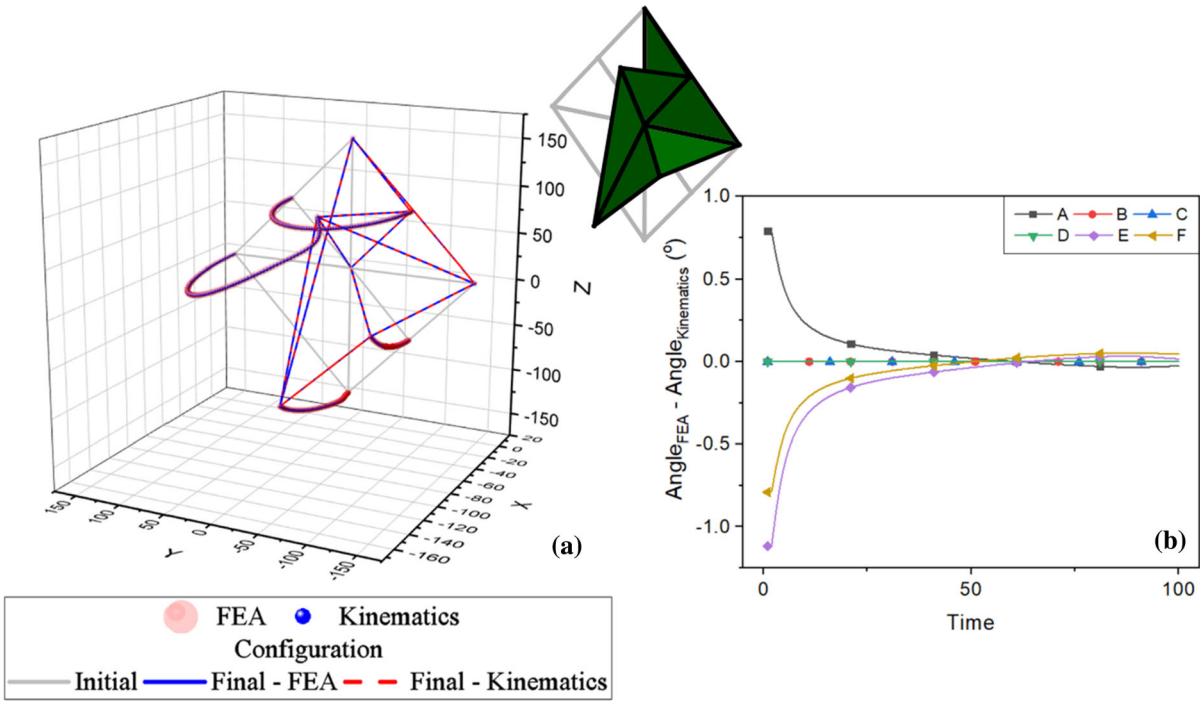

Fig. 13 Asymmetric behavior of the waterbomb cell described by the kinematic formulation (using D–H parameters) and the FEA formulation (using bar-and-hinge description). **a** Tridimensional movement of the cell on folding process; **b** difference between the inner angles evaluated by kinematics method and by FEA method

symmetrically actuated by considering that the cells are pulled radially through the middle vertex of each unitary cell (point *O* in Fig. 2). Longitudinal symmetry is placed on the unit cells vertex, in such a way that the radius of each line measured from the tessellation axis to the vertex (point *O* in Fig. 2) is the same between lines and within the same line.

This analysis is performed in two stages: the first study evaluates the influence of the number of lines (m) considering a tessellation with $n = 6$ cells on each line; the second study evaluates the influence of the number of cells on each line (n) considering two tessellations: with $m = 5$ lines and with $m = 6$ lines.

In order to evaluate the influence of the number of lines (m), four tessellations formed by waterbomb unit cells on each line are of concern varying the numbers of lines (Fig. 15): lines (Fig. 15a); lines (Fig. 15b); lines (Fig. 15c) and lines (Fig. 15d). For all tessellations, initial configuration is the opened one (gray color). Figure 15 shows each tessellation in a final closed configuration. The purpose of the analysis is to evaluate the behavior of each individual waterbomb unit cell when the structure is folded in a symmetric way. In order to visualize any local asymmetry, the inner angles are represented according to the previous cases: Π_1, Π_2 and Π_3.

This first set of simulations is represented in Fig. 16, by a relation between the inner angles of each one of the cells. The inner angles are represented according to the relation of Π_2. Therefore, they are plotted as: A versus C, D versus F and B versus E, where the bisector line represents the symmetric case (Π_3). Figure 17 shows, respectively, the inner angle relation for the tessellation with lines (Fig. 17a), lines (Fig. 17b), lines (Fig. 17c) and lines (Fig. 17d).

Two major observations can be made about these cases. The first one is related to the influence of the tips or endings in this tessellation. Note that this tessellation has free ends, where at least 6 vertices on the top (related to vertex *E*) and at least 6 vertices on the bottom (related to vertex *B*) are not restrained in any way, and an inversion of crease type (from mountain to valley fold) might occur freely. Besides, these free endings result in additional degrees of freedom, even when a controlled symmetric folding process is performed. The tip influence can be seen on all four

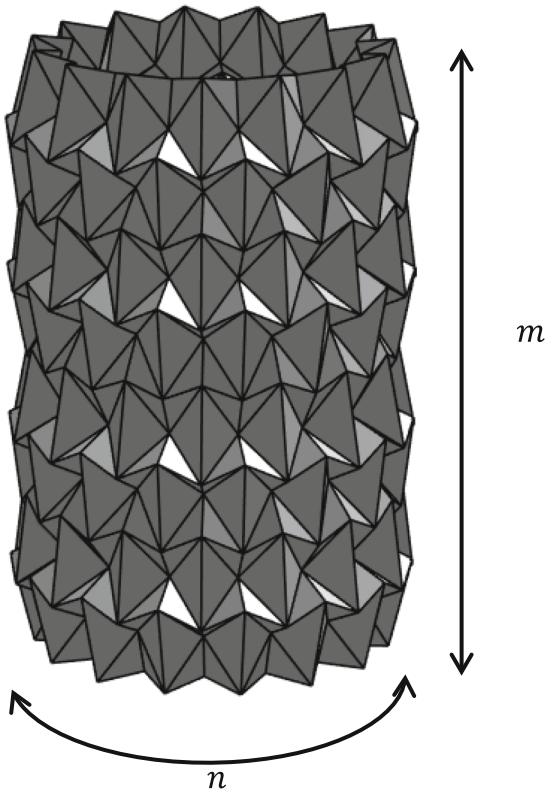

Fig. 14 Closed waterbomb tessellation generated with the 6 creased waterbomb unit cell. The tessellation is defined by the number of lines (m) and the number of cells on each line (n)

graphs by the deviance of both vertices B and E from the symmetric condition (case Π_3). Note that for all four cases, the first and the last lines, associated with the bottom and the top of the tessellation, behave according to case Π_2, while the lines contained within the first and the last one tends to behave according to Π_3. This analysis comes from the observation of the points places outside the bisector line.

The second observation is related to the influence of the number of lines in the structure behavior. Specifically, the waterbomb cell in the tessellation with and odd number of lines (Fig. 15a, c) presents a plane-symmetric behavior (according to case Π_2) for all cells on the first and last lines (Fig. 16a, c), while it presents a symmetric behavior (case Π_3) for the remaining lines. On the other hand, the waterbomb in the tessellation with and even number of lines (Fig. 15b, d) tends to behave in a plane-symmetric condition (according to case Π_2), with a more prominent plane-symmetry occurring on the external lines (first and last one) and a more prominent symmetry occurring on the other lines (Fig. 16b, d).

The second study evaluates the influence of the number of cells on each line on the structure behavior during the folding process. For this study, a series of tessellations are considered, going from 6 cells per line until 22 cells per line. As observed in Fig. 16a–d, the major deviance occurs on the first and last lines, because of the endings. Concerning the influence of the number of cells on the symmetric behavior of the inner lines, it is necessary to focus on the line that presents the major deviance from the symmetric behavior (case Π_3) for each simulation, neglecting the first and the last lines (ending effect). In addition, it should be pointed out that there is a point for each simulation where this deviance reaches its maximum value, as can be seen in Fig. 16a–d. Figure 17 brings the maximum deviance observed for each case, going from to. Figure 17a shows this evaluation for a tessellation with an odd number of lines (m = 5 lines), while Fig. 17b shows the deviance for a tessellation with an even number of lines (m = 6 lines). The deviance is evaluated as the absolute difference between the angles of a cell on the line m and a cell on the line $mn/2$, for the tessellation with an even number of lines, and on the line $m(n+1)/2$, for the tessellation with an odd number of lines.

It is noticeable that the tessellation with an odd number of cells (Fig. 17a) presents the maximum absolute deviance that tends to grow linearly with the increase of the number of cells per line. Besides, all cells outside the central line $m(n+1)/2$ behave according to the Π_2 plane-symmetric case. It is also noticeable that for a tessellation with up to 10 cells per line, the maximum deviance observed is around 1°. The combined result from simulation presented at Fig. 16a, c and the simulation presented in Fig. 17a indicates that for a tessellation with an odd number of lines and a maximum of 10 cells per line, a simplified model describing the unit cell behavior, such as the trigonometric formulation presented as Sect. 4, can be extrapolated as representative of the structure behavior, and the influence of the endings is contained within the cells from the first and the last line. In addition, a tessellation with an even number of cells per line (Fig. 17b) presents a significant deviance from the symmetric behavior (case Π_3). In opposition to the result presented in Fig. 17a, Fig. 17b indicates a smoother increasing of the maximum deviance.

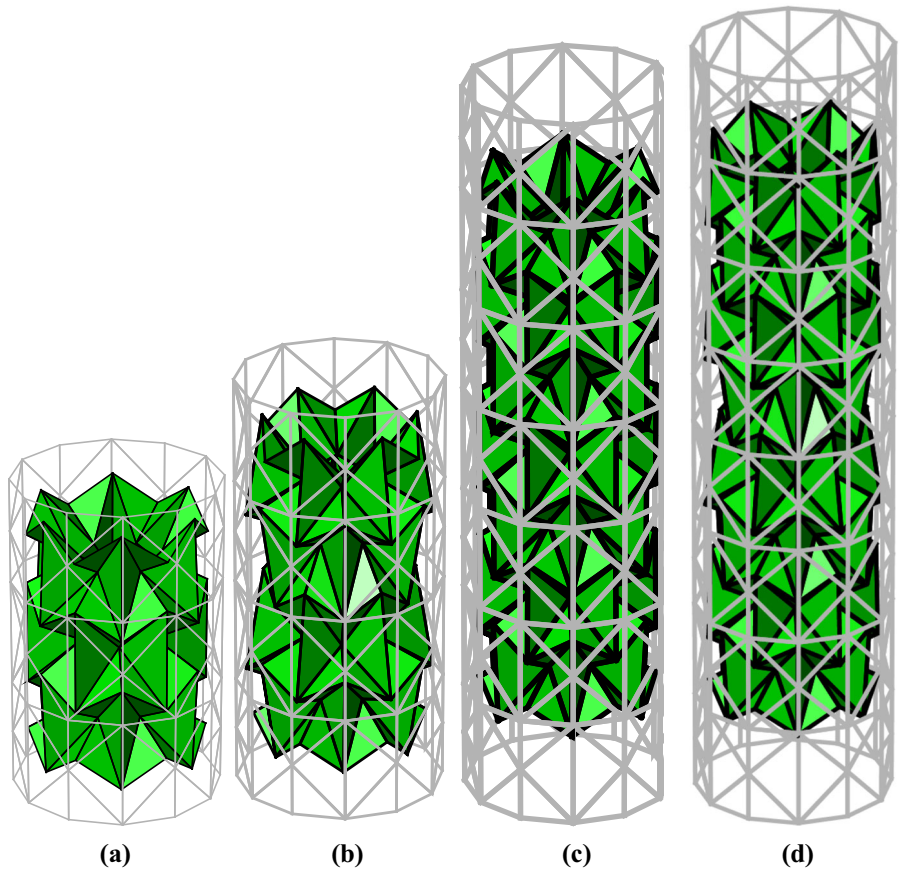

Fig. 15 Closed waterbomb tessellation formed by m lines, with each line composed by n = 6 squared cells. **a** m = 3; **b** m = 4; **c** m = 7; **d** m = 8

Besides, the increase of the number of cells causes the loss of the circumferential symmetry. This fact is due to the folding process that occurs on the tessellation.

The natural force (Fig. 1b) associated with the folding process of the closed tessellation evaluated in Fig. 17 tends to generate a ball-shaped origami, where the middle lines tend to present a symmetric behavior, and the endings tend to be asymmetric. On the other hand, if this natural force (Fig. 1b) tends to generate a cylindrical-like origami, a different behavior is observed, where the middle lines tend to present an asymmetric behavior and the endings tend have a symmetric behavior.

The folding process of a cylindrical-like origami is shown in Fig. 18. The structure presents a motion that can be translated as a circumferential reduction, followed by an axial compression, a strangulation, and an axial relaxation. This motion sequence is presented at Fig. 18a, for a tessellation with $m = 5$ lines, and at Fig. 18b, for a tessellation with $m = 6$ lines. Note that the strangulation is more prominent on the tessellation with an even number of lines (Fig. 18b).

The strangulation effect is further explored by considering an index, Δ, expressed by the difference between the tessellation radius measured from the middle axis to the vertex B of a cell in the middle line and the tessellation radius measured from the tessellation axis to the vertex B of a cell in the first line. Thus, $\Delta = 1$ means that the tessellation does not present a strangulation, having a cylindrical surface (zero Gaussian curvature). On the other hand, $\Delta \neq 1$ means that the tessellation presents a strangulation that can be a positive Gaussian curvature ($\Delta > 1$) or a negative Gaussian curvature ($\Delta < 1$). It is important to notice that closed waterbomb tessellations with an even number of lines always presents a negative Gaussian curvature under symmetrical actuation,

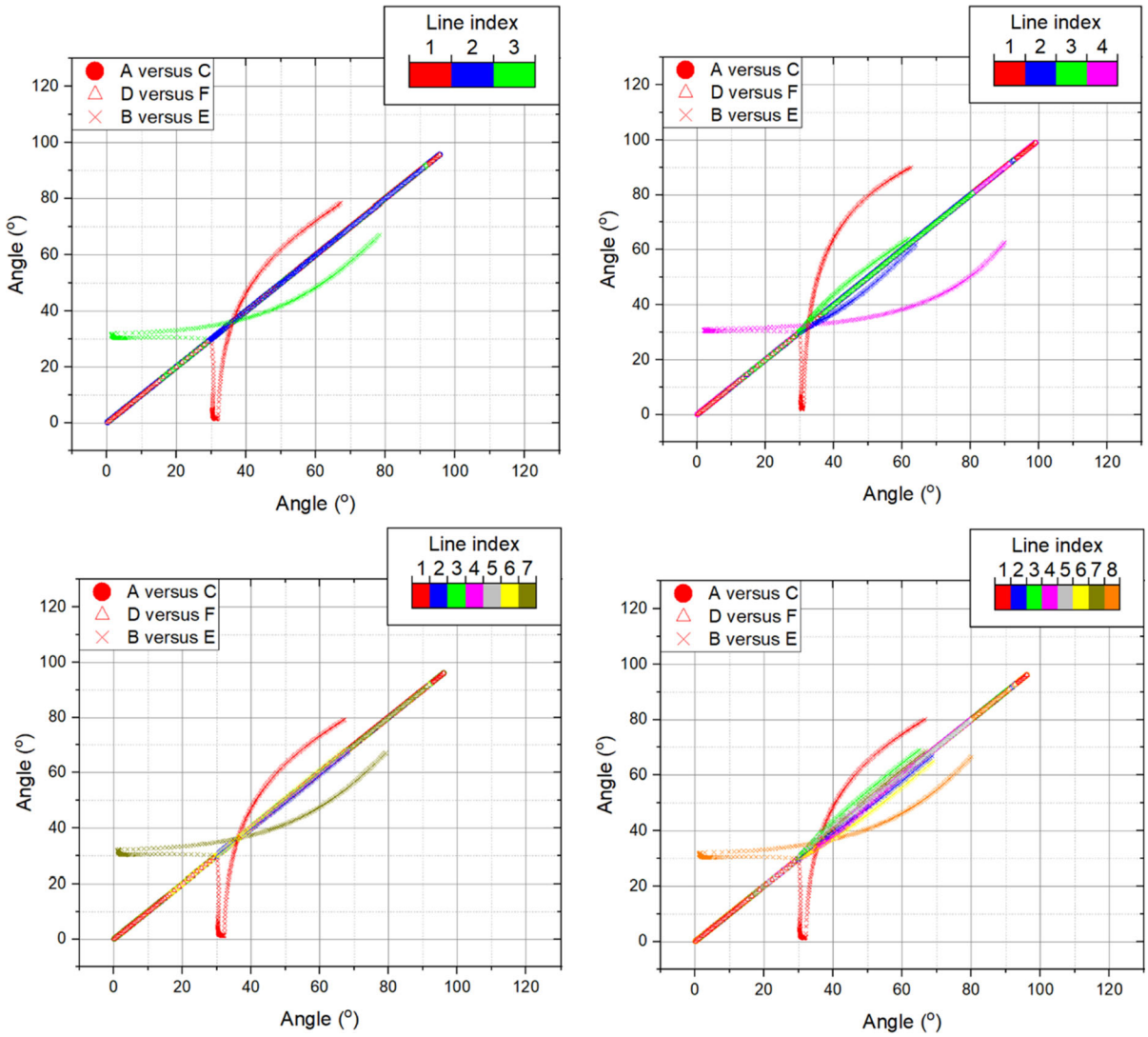

Fig. 16 Relation between the inner angles of each one of the 6L cells of the tessellation, where m is the number of lines of that tessellation. **a** Relation for the case m = 3, **b** Relation for the case m = 4, **c** relation for the case m = 7, and **d** Relation for the case m = 8. For all four cases, the bisector line represents the symmetric behavior (case Π_3)

which is an important consideration when designing closed waterbomb tessellations. Figure 19 presents the relation between the number of origami lines (m) and its even/odd parity with the prominence of the strangulation effect. It is clear that the origamis with even number of lines have a greater strangulation effect.

Figure 20 presents the influence of the number of cells on each line (n) on the strangulation effect (Δ), for both even and odd closed waterbomb tessellations. Figure 20 also brings the information regarding the influence of the number of lines (m). The first important thing to be noticed is that the parity of lines (m odd or even) of the tessellation seems to be more expressive in the strangulation than the number of lines itself (m). For a fixed number of cells on each line (n), the tessellation with an even number of lines (m) always presents a negative Gaussian curvature. Besides, the increase of the number of lines (m) does not have an expressive influence on the strangulation effect (Δ), apart from the increasing from $m = 3$ to $m = 5$ that stands out. A similar analysis is made on the tessellation with an odd number of lines, where the increase of the number of lines slightly changes the

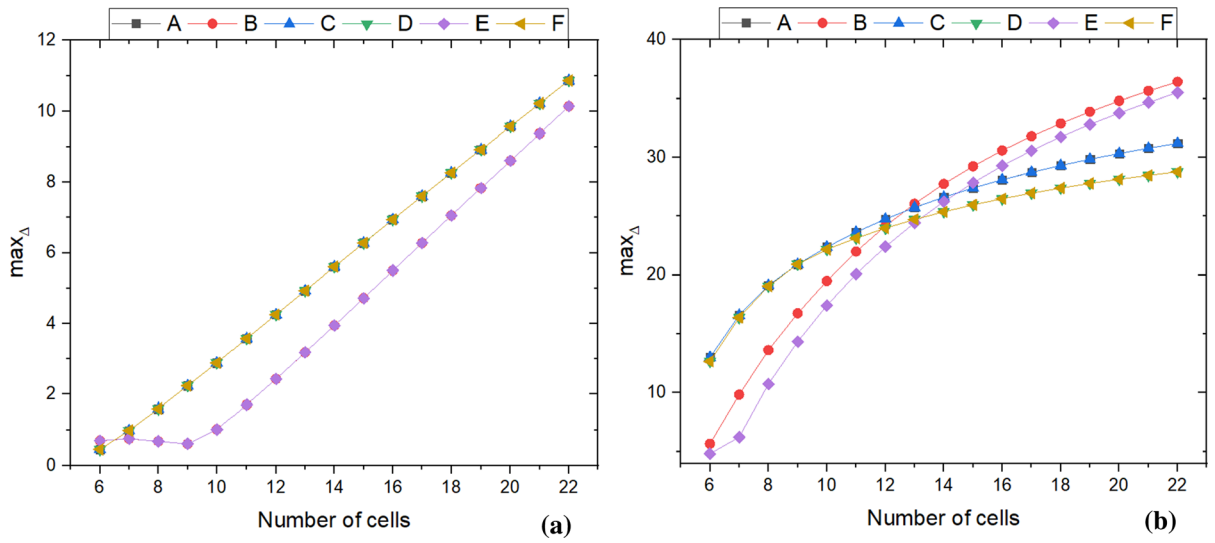

Fig. 17 Maximum deviation of each inner angle with the increasing of the number of cells per line, considering a tessellation with m lines. **a** Maximum deviation for a tessellation with an odd number of lines, with m = 5; **b** Maximum deviation for a tessellation with an even number of lines, with m = 6

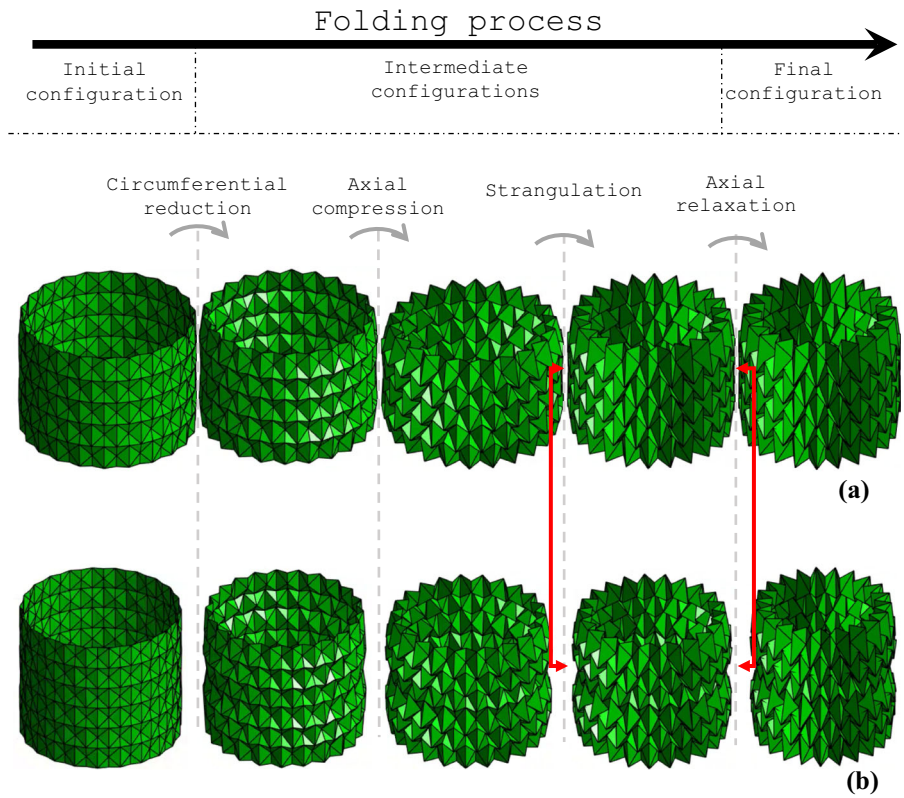

Fig. 18 Folding process of a tessellation with m = 5 lines (**a**) and m = 6 lines (**b**), with each remarkable phase highlighted. The strangulation that happens in the middle of the tessellation is highlighted by red arrows

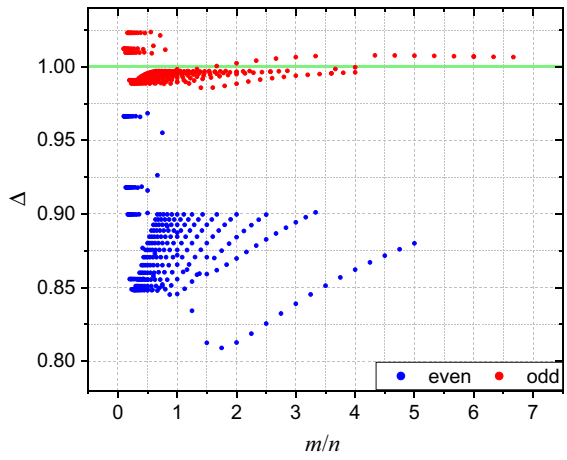

Fig. 19 Evaluation of the strangulation effect (Δ) for even and odd tessellation, as a function of the ratio between the number of lines (m) and the number of cells on each line (n)

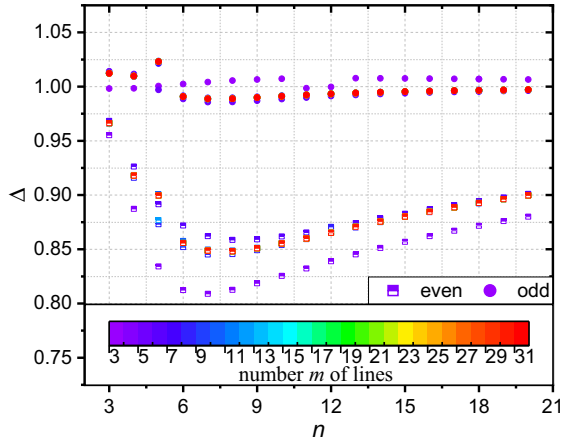

Fig. 20 Strangulation (Δ) evaluation for both even and odd tessellations as a function of the number of cells on each line (n), with a color map on the number of lines (m)

curvature of the outer surface of the closed waterbomb tessellation, varying between positive ($\Delta > 1$) and negative ($\Delta < 1$) Gaussian curvature. The increase of the number of lines in cases where $m < 6$ can be an improvement for applications such as stents, since a positive Gaussian curvature surface does not present a gap. Cases where $m \geq 6$, however, tends to generate an unfolded closed waterbomb tessellation with a negative Gaussian curvature, which generates the gap on the middle line. The increase of the number of cells on each line (n) does not present a significant influence on the tessellation with an odd number of lines for cases where $n > 5$. Nevertheless, the number of cells on each line (n) significantly influences the strangulation effect (Δ), reducing its expressivity with the increasing on the number of lines (m).

6 Conclusions

This paper presents an investigation of the origami waterbomb pattern from its unit cell, exploring different formulations for origami structures. Two approaches are presented: kinematics based on equivalent mechanism; and mechanical based on finite element analysis (FEA). Kinematics analysis is based on rigid hypothesis where all deformations occur on creases and the panel is rigid, defining a reduced-order model. A global investigation is performed, evaluating the tridimensional behavior of the unit cell under symmetric and asymmetric conditions. Mechanical analysis considers asymmetric situations and non-rigid cases as well. Numerical simulations show that a reduced order model formulation is justified and applicable, and its range of validity can be established by the FEA. A closed tessellation analysis is performed considering symmetric actuation showing that the structure presents a strangulation effect that is more prominent for tessellations with an even number of lines. This strangulation affects a small region of the tessellation where the unit cells present a quasi-symmetric or plane-symmetric behavior. A tessellation with an odd number of lines tends to present both local and global symmetries and, for a tessellation with a minimum of five lines, neither the increase of the number of lines nor the increase of the number of cells on each line has a significant effect on the strangulation effect. This information is important for a design strategy and for the use of reduced-order models.

Acknowledgements The authors would like to acknowledge the support of the Brazilian Research Agencies CNPq, CAPES and FAPERJ.

Declaration

Conflict of interest The authors declare that they have no conflict of interest.

Appendix

This appendix presents details about the origami formulation.

Equivalent mechanism analysis

The waterbomb unit cell is a closed-loop mechanism and, for the formulation used in this paper, it is assumed that the first linkage $(i = 1)$ is associated with the crease OB, being numbered counterclockwise. Therefore, the last linkage $(i = 6)$ is related to the crease OA (see Fig. 2). The frame definition is summarized as:

1. The first frame $(i = 1)$ is defined as the crease OB.
2. Frames are disposed following a counterclockwise sequence, following the vertex order B, C, D, E, F and A, starting from $(i = 1)$ at vertex B and ending at $(i = 6)$ at vertex A.
3. The z_i axis of each i frame is aligned with the crease, with the origin at O (see Fig. 2).
4. The y_i axis of each frame is coplanar with the origami face delimited by the joints i and $i - 1$, and the y_1 frame is coplanar with the origami face delimited by frames 1 and 6.
5. The x_i axis of each i frame is the normal of the face delimited by joints i and $i - 1$, and the x_1 frame is the normal to the face delimited by frames 1 and 6.
6. The waterbomb defines an inner region and an outer region, where the inner region is contained within the waterbomb edges AB, BC, CD, DE, EF and FA. Each x_i axis points outwards the inner region.

Each z_i axis is defined such that every θ_i angle belongs to the range $[0, \pi]$. With this consideration, z_i axis associated with valley folds (creases OA, OC, OD and OF) are positioned along the crease, pointing from O_i to the correspondent vertex (A, C, D or F), while z_i axis associated with mountain folds (OB and OE) are positioned along the crease, pointing to the opposite direction of the correspondent vertex (B or E). The values of the D–H parameters for a generic waterbomb cell are given in Table 3.

The waterbomb pattern has a characteristic that all joints intercept at a common point (point O in Fig. 2), resulting in $a_i = R_i = 0\,(i = 1, \ldots 6)$. In addition, α_i is fixed for each pair of consecutive joints, being associated with the angle λ that defines the shape of the waterbomb cell wherein, for a squared waterbomb cell, $\lambda = \pi/4$.

Table 3 D–H parameters and its correspondence to each vertex of the unit cell

Vertex	B	C	D	E	F	A
i	1	2	3	4	5	6
α_i	$\pi - \lambda$	$\pi + 2\lambda$	$\pi - \lambda$	$\pi - \lambda$	$\pi + 2\lambda$	$\pi - \lambda$
θ_i	θ_1	θ_2	θ_3	θ_4	θ_5	θ_6
R_i	0	0	0	0	0	0
a_i	0	0	0	0	0	0

Finite element analysis

The behavior of origami structures is described assuming quasi-static equilibrium, where the shape change is due to a succession of equilibrium configurations. It is assumed that the total potential energy Φ is the sum of the strain energy stored in bars, U_{bar}, the strain energy stored in folding (torsional springs on the creases) and bending (torsional springs as virtual folds), U_{spr}, the work done by external loads, V_{ext},

$$\Phi = U_{bar} + U_{spr} - V_{ext} \tag{8}$$

By considering quasi-static equilibrium, the ith bar element is represented by

$$\begin{aligned} \boldsymbol{T}^i_{bar} &= A_i L_i S_x \frac{\partial E_x}{\partial \boldsymbol{u}_i} \\ \boldsymbol{K}^i_{bar} &= A_i L_i \left[S_x \frac{\partial^2 E_x}{\partial \boldsymbol{u}_i^2} + C \frac{\partial E_x}{\partial \boldsymbol{u}_i} \left(\frac{\partial E_x}{\partial \boldsymbol{u}_i} \right)^T \right] \end{aligned} \tag{9}$$

where S_x is the second Piola–Kirchhoff (P–K) tensor, C is a tangent modulus, A_i is the transversal section area of the bar element and L_i is the length of the bar element. The degree of freedom that describes the torsional spring (its rotation) is given by the dihedral angle between the panels and can be obtained straight from the displacements and the original coordinates of the vertices. Besides, the torsional spring has its behavior assumed as linear elastic. Thus, for the jth torsional spring,

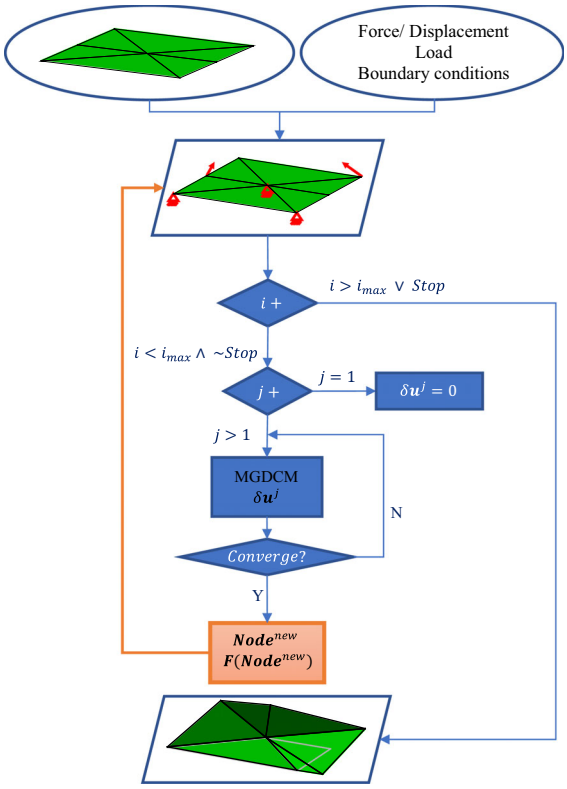

Fig. 21 Overview of simulation framework. The initial configuration is inserted in a combination of Nodes and Bars, and the external forces and constraints are carefully considered. At each iteration, a convergence is performed on each node displacement using MGDCM, and, after converging, a new input is generated with the revaluation of the forces based on the new Nodes (Nodes considering the displacement)

$$\begin{aligned} \boldsymbol{T}^{j}_{spr} &= L_j \frac{\partial \Psi}{\partial \theta}\frac{\partial \theta}{\partial \boldsymbol{u}_j} L_j M_{RES}\frac{\partial \theta}{\partial \boldsymbol{u}_j} \\ \boldsymbol{K}^{j}_{spr} &= L_j \left[M_{RES}\frac{\partial^2 \theta}{\partial \boldsymbol{u}_j^2} + k\frac{\partial \theta}{\partial \boldsymbol{u}_j}\left(\frac{\partial \theta}{\partial \boldsymbol{u}_j}\right)^T \right] \end{aligned} \tag{10}$$

where M_{RES} is the resisting moment per unit length, k is the rotational stiffness modulus per unit length, Ψ is the stored energy function and θ is the dihedral angle. The linear formulation of the moment M_{RES} does not detect local penetration of origami panels and, to avoid that, additional kinematic constraints are considered. Based on that, the moment per unit length is given by

$$M_{RES} = \begin{cases} k(\theta_1 - \theta_0) + \left(\frac{2k\theta_1}{\pi}\right)\tan\left(\frac{\pi(\theta-\theta_1)}{2\theta_1}\right) & , \theta \in \,]0, \theta_1[\\ k(\theta - \theta_0) & , \theta \in [\theta_1, \theta_2] \\ k(\theta_2 - \theta_0) + \left[\frac{2k(2\pi-\theta_2)}{\pi}\right]\tan\left(\frac{\pi(\theta-\theta_2)}{4\pi-2\theta_2}\right) & , \theta \in \,]\theta_2, 2\pi[\end{cases} . \tag{11}$$

The original Merlin Code assumes that the load is applied with respect to the undeformed configuration, keeping its initial characteristic during all time steps. Here, this input load follows the deformed configuration and therefore, follows the node movement. This approach allows a proper description of the origami that does not present any incorrect extra stretching. A workflow for the modified FEA is presented in Fig. 21, illustrated by a single cell. The *XYZ* coordinates of each node of the origami is used as input, being reshaped as a combination of nodes and panels, and the creases are properly identified and stored as bars in a trussed-like structure. Additionally, the boundary conditions and the actuation are defined as inputs, being either force or displacement type. This set of inputs are fed to the solver that, using an iteration method and with the formulation previously presented, converge the solution through a quasi-static analysis of the unbalanced system, until it reaches the equilibrium.

References

1. Belcastro SM, Hull TC (2002) Modeling the folding of paper into three dimensions using affine transformations. Linear Algebra Appl 348:273–282
2. Bowen LA, Baxter WL, Magleby SP, Howell LL (2014) A position analysis of coupled spherical mechanisms in action origami. Mech Mach Theory 77:13–24
3. Chen Y, Feng H, Ma J, Peng R, You Z (2016) Symmetric waterbomb origami. Proc R Soc A Math Phys Eng Sci 472(2190):20150846
4. Chen BG-G, Santangelo CD (2018) Branches of triangulated origami near the unfolded state. Phys Rev X 8(1):011034
5. Chiang CH (2000) Kinematics of spherical mechanisms. Krieger Publishing Company, Malabar
6. Denavit G, Hartenberg R (1955) A kinematic notation for lower pair mechanics based on matrices. J Appl Mech 22:215–221
7. Evans TA, Lang RJ, Magleby SP, Howell LL (2013) Rigidly foldable origami twists. In: Origami 6, AMS, vol 1, pp 119–130
8. Figueredo LFC, Adorno BV, Ishihara JY, Borges GA (2013) Robust kinematic control of manipulator robots using dual

quaternion representation. In: IEEE international conference on robotics and automation, Karlsruhe, pp 1949–1955
9. Fonseca LM, Rodrigues GV, Savi MA, Paiva A (2019) Nonlinear dynamics of an origami wheel with shape memory alloy actuators. Chaos Solitons Fractals 122:245–261
10. Fonseca LM, Savi MA (2020) Nonlinear dynamics of an autonomous robot with deformable origami wheels. Int J Non-Linear Mech 125:103533
11. Gardiner M, Aigner R, Ogawa H, Hanlon R (2018) Fold mapping: parametric design of origami surfaces with periodic tessellations. In: 7th origami science mathematics and education conference, vol 1, pp 105–118
12. Gattas JM, You Z (2014) Quasi-static impact of indented foldcores. Int J Impact Eng 73:15–29
13. Gogu G (2004) Chebychev–Grübler–Kutzbach's criterion for mobility calculation of multi-loop mechanisms revisited via theory of linear transformations. Eur J Mech A Solids 24(3):427–441
14. Huang C, Chen C (1995) The linear representation of the screw triangle—a unification of finite and infinitesimal kinematics. ASME J Mech Des 117(4):554–560
15. Kresling B, Abel R, Robert JC (2008) Natural twist buckling in shells: from the Hawkmoth's bellows to the deployable KRESLING-pattern and cylindrical Miuraori. In: Abel JF, Cooke JR (eds) Proceedings of the 6th international conference on computation of shell and spatial structures, Ithaca
16. Kuribayashi K, Tsuchiya K, You Z, Tomus D, Umemoto M, Ito T, Sasaki M (2006) Self-deployable origami stent grafts as a biomedical application of Ni-rich TiNi shape memory alloy foil. Mater Sci Eng A 419:131–137
17. Lang RJ (1996) A computational algorithm for origami design. In: Proceedings of the twelfth annual symposium on computational geometry, pp 98–105
18. Lang RJ (2011) Origami design secrets: mathematical methods for an ancient art. CRC Press, Alamo
19. Lee SH, Kim WK, Oh SM, Yi BJ (2005) Kinematic analysis and implementation of a spherical 3-degree-of-freedom parallel mechanism. In: Proceedings of 2005 IEEE/RSJ international conference on intelligent robots and systems, pp 972–977
20. Leon S, Paulino GH, Pereira A, Lages EN (2011) A unified library of nonlinear solution schemes. Appl Mech Rev 64(4):040803
21. Leon S, Lages EN, de Araújo CN, Paulino GH (2014) On the effect of constraint parameters on the generalized displacement control method. Mech Res Commun 56:123–129
22. Liu K, Paulino GH (2017) Nonlinear mechanics of non-rigid origami: an efficient computational approach. Proc R Soc A Math Phys Eng Sci A 473:20170348
23. Lv C (2016) Theoretical and finite element analysis of origami and kirigami based structures, THESIS
24. Ma J, Feng H, Chen Y, Hou D, You Z (2020) Folding of tubular waterbomb. Research 2020, Article ID 1735081
25. Mavroidis C, Dubowsky S, Drouet P, Hintersteiner J, Flanz J (1997) A systematic error analysis of robotic manipulators: application to a high performance medical robot. In: Proceedings of international conference on robotics and automation, Albuquerque, NM, USA, vol 2, 1997, pp 980–985
26. Ogden RW (1997) Non-linear elastic deformations. Dover Publications, New York
27. Rodrigues GV, Fonseca LM, Savi MA, Paiva A (2017) Nonlinear dynamics of an adaptive origami-stent system. Int J Mech Sci 133:303–318
28. Rodrigues GV, Savi MA (2021) Reduced-order model description of origami stent built with waterbomb pattern. Int J Appl Mech 13(2):2150016
29. Schenk M, Guest SD (2011) Origami folding: a structural engineering approach. In: Wang-Iverson P, Lang RJ, Yim M (eds) Origami 5. CRC Press, Boca Raton, pp 293–305
30. Song J, Chen Y, Lu G (2013) The thin-walled tubes with origami pattern under axial loading. In: JSST 2013 international conference on simulation technology
31. Struik DJ (1961) Lectures on classical differential geometry, 2nd edn. Addison-Wesley Pub Co, Reading
32. Tachi T (2010) Geometric considerations for the design of rigid origami structures. In: Proceedings of the international association for shell and spatial structures symposium 2010, Shanghai, China
33. Tachi T (2012) Design of infinitesimally and finitely flexible origami based on reciprocal figures. J Geom Graph 16(2):223–234
34. Tachi T (2013) Freeform origami tessellations by generalizing Resch's patterns. In: Proceedings of ASME IDETC/CIE (symposium on origami-based engineering design), DETC2013-12326, Portland, USA, August 4–7
35. Turner N (2015) A review of origami applications in mechanical engineering. Proc Inst Mech Eng C J Mech Eng Sci 230(14):2345–2362
36. Zhao Y, Endo Y, Kanamori Y, Mitani J (2018) Approximating 3D surfaces using generalized waterbomb tessellations. J Comput Des Eng 5:442–448